View Article Online / Journal Homepage / Table of Contents for this issue

Published on 03 July 2002. Downloaded by Kyoto Daigaku on 09/09/2016 06:22:43.

11 State-to-state rotational inelastic scattering of free radicals

Hiroshi Kohguchi[a] **and Toshinori Suzuki***[a,b,c]

[a] *Institute for Molecular Science and The Graduate University for Advanced Studies, Okazaki, Myodaiji 444-8585, Japan*
[b] *Chemical Dynamics Laboratory, RIKEN, Hirosawa, Wako 351-0198, Japan. E-mail: suzuki@ims.ac.jp*
[c] *PRESTO, Japan Science and Technology Corporation, Kawaguchi, Saitama, Japan*

1 Introduction

Free radicals play important roles in a vast area of chemistry, and great efforts have been devoted to their structural and dynamic studies. Having unpaired electrons, free radicals are accompanied by closely-lying electronic states, which inevitably give rise to multi-surface non-adiabatic collision dynamics beyond the Born–Oppenheimer approximation.

Rotational inelastic scattering (RIS) is the simplest scattering process of free radicals without a chemical change. However, it captures the essential feature of multi-surface dynamics with various quantum interference effects. Furthermore, this is the only scattering process of radicals for which highly accurate quantum mechanical computations and detailed experimental investigations at the state-to-state level are currently available. Full elucidation of RIS through critical comparison of the most advanced theory with experiments will establish a firm basis for elucidating reactive scattering of free radicals to be accomplished in the future. RIS attracts further attention in relation to other research fields. For instance, it has been speculated to be an excitation mechanism of interstellar OH radicals that create maser radiation, as observed by radio astronomy. Mysterious strong maser lines indicate that there is population inversion among the OH rotational levels, however, the pumping mechanism has yet to be concluded.

This article reviews the latest experimental investigations on RIS of free radicals, the neutral molecules with unpaired electrons, with atomic and diatomic projectiles. Due to the limited length of the article, theoretical frameworks are only briefly explained. We attempt to list much excellent literature for readers who are interested in a more thorough explanation of the theories and also detailed historical backgrounds.

View Article Online

Published on 03 July 2002. Downloaded by Kyoto Daigaku on 09/09/2016 06:22:43.

(i) High-resolution probing of interaction potentials

Free radicals have complex energy level structures for unquenched electronic orbital and spin angular momenta and their interactions with nuclear rotational angular momentum. Post-collision quantum states of radicals are determined by complicated interference effects in multi-surface dynamics, so their population and scattering distributions are strongly dependent on the final quantum state. Therefore, experimental investigation absolutely requires state-resolved detection of the final quantum states, in other words, laser detection of products. This is experimentally highly demanding in that the number density of detectable products is dramatically reduced by state-selection. The limited spatial and temporal width of a laser beam further reduces the signal level, since only a fraction of scattered particles would be photoexcited. Multiplex detection is an extremely important solution for this problem, as discussed later, and further experimental improvements towards higher sensitivity and resolution should certainly be pursued.

The nuclear dynamics on multiple potential energy surfaces is expressed by coupled equations and is solved by time-dependent (wave packet) or time-independent (close-coupling) methods. The most sensitive probe of collision dynamics is the angular distribution of a state-selected product, termed as the state-resolved differential cross section (SR-DCS). This quantity has usually been obtained by the close-coupling method. In the past when computational power was limited, various dynamical approximations were made on the coupled equations to reduce the computation time and the memory space required, however, these approximations are no longer necessary. The accuracy of the close-coupling calculations directly reflects the quality of the potential energy surfaces (PESs) provided by quantum chemistry. Such an ultimate level of detail has been achieved, for example, for the NO + Ar system. As long as the nuclear dynamics is treated properly, the scattering problem is reduced to examination of the quality of the PESs.

Note that some features of RIS are governed by the difference between the two PESs. This implies that the magnitude of an effective interaction potential will be of the order of cm^{-1} (or meV). Generally, the accuracy of a PES must be better than 1 kcal mol^{-1} (350 cm^{-1}) for a qualitatively correct description of chemical reactions, since an error of 1 kcal mol^{-1} in the potential barrier height leads to one order of magnitude difference in the reaction rate at 300 K. The RIS is regarded as an extremely critical examination of the interaction potentials at *spectroscopic* accuracy. In reactive scattering experiments, such a high-precision may be expected only for state-of-the-art investigations on the benchmark systems F + H_2 (ref. 1) and H + H_2.(ref. 2)

An RIS experiment exploring the interaction potentials with a positive energy above the asymptotic state is complementary to the spectroscopy of van der Waals (vdW) complexes with negative energy. In principle, RIS samples both the attractive and repulsive parts of the PESs in that it should carry all the information of the PESs. In reality, however, scattering experiments inevitably suffer from the insuppressible width of the collision energy originating from the finite molecular beam speed spreads, which wash out some delicate fingerprints in the scattering distributions. Complexity also arises from uncontrollable mutual orientation angles of the projectiles in the systems larger than diatom–diatom. Thus, for examination of the potential

View Article Online

well, spectroscopy of vdW complexes is more straightforward. In either case, comparison with highly accurate quantum mechanical computations is the key to extracting full information from the experimental observable. We will describe briefly the theoretical framework in the next section.

Published on 03 July 2002. Downloaded by Kyoto Daigaku on 09/09/2016 06:22:43.

(ii) Close-coupling calculations

Rigorous theory for RIS of free radicals has been developed gradually by contributions from a number of researchers, and the most complete form is perhaps that by Alexander and co-workers.[3–8] Program suites[9,10] are now available for predicting scattering and bound states of free radicals in each electronic state ($^{2S+1}\Lambda$) interacting with an atom. We describe here the machinery briefly for a $^2\Pi$ molecule colliding with a structureless atom.

The double degeneracy of the $^2\Pi$ electronic state of a radical is lifted by interactions with an atom in non-linear configurations. The two states thus created will have A′ or A″ symmetry with respect to the reflection through the molecular plane. When an atom approaches either parallel or perpendicular to a pπ lobe of an electron (or an electron hole), the system becomes one of these A′ or A″ states. On the other hand, since an atom does not necessarily approach parallel or perpendicular to the pπ lobe but rather from intermediate angles, the system in collision generally becomes a superposition of the A′ and A″ electronic states. The phase shifts between the scattering wave functions in these two states determine the cross sections of the fine structure conserving, $^2\Pi_{1/2}$–$^2\Pi_{1/2}$ and $^2\Pi_{3/2}$–$^2\Pi_{3/2}$, and changing processes, $^2\Pi_{1/2}$–$^2\Pi_{3/2}$.

In the Hund's case (a) basis where appropriate symmetry properties are taken into account, the wave function of the $^2\Pi$ state is expressed by $|jm_j\Omega\varepsilon\rangle$, where m_j and Ω denote projections of the angular momentum j onto a spatial axis and a molecular axis, respectively. A further symmetry property to note is the rotationless parity index ε represented by *e*/*f* labeling ($\varepsilon = +1$ for the *e*-state, and $\varepsilon = -1$ for the *f*-state) for the Λ-doublet, which is the parity obtained by omitting a rotation-dependent phase factor $(-1)^j$ from the total parity. The Hamiltonian ($\hat{H}$) for the total system is described in Jacobi coordinates (r,R,θ) as follows,

$$\hat{H}(R,\theta) = \frac{\hbar^2}{2\mu R^2}\frac{\partial}{\partial R}R^2\frac{\partial}{\partial R} + \frac{L^2}{2\mu R^2} + V(R,\theta), \qquad \text{(I-1)}$$

where the diatomic bond length (r) was excluded under the rigid rotor approximation. A time-independent wave function of a scattering state ($\Psi(\boldsymbol{R})$) can be decomposed into a radial ($R = |\boldsymbol{R}|$) and an angular ($\boldsymbol{R}/R$) part as follows;

$$\Psi^{JM}(R) = \frac{1}{R}\sum_{jL\Omega\varepsilon} C^{JM}_{jL\Omega\varepsilon}(R)\left|jL\Omega\varepsilon JM\right\rangle \qquad \text{(I-2)}$$

The angular part, $|jL\Omega\varepsilon JM\rangle$, is a coupled basis function composed of the molecular eigenstates of a radical and the relative orbital motion between the radical and an atom; the angular momentum of the relative orbital motion ($\boldsymbol{L}$) and the angular momentum of a free radical ($\boldsymbol{j}$) compose the total angular momentum ($\boldsymbol{J}$) of the whole

View Article Online

system, $\boldsymbol{J} = \boldsymbol{j} + \boldsymbol{L}$. The radial part, $C^{JM}_{jL\Omega\varepsilon}(R)$, acts as an expansion coefficient for the angular basis function.

Using eqn. (I-1) and (I-2), the Schrödinger equation is transformed to a close-coupling equation expressed in the following matrix form.

$$\left(\frac{\mathrm{d}^2}{\mathrm{d}R^2} + \boldsymbol{W}(R)\right)\boldsymbol{C}^J(R) = \boldsymbol{0} \tag{I-3}$$

The elements of the matrix $\boldsymbol{W}(R)$ include the centrifugal terms and the interaction potential terms, the latter of which create off-diagonal elements between the coupled $|j\Omega\varepsilon LJM\rangle$ basis functions. Eqn. (I-3) is solved for $\boldsymbol{C}^J(R)$ by a numerical propagation from a small towards a large value of R. The propagation starts from a sufficiently small value in the classically forbidden region and with the initial condition of $\boldsymbol{C}^J(R_{\mathbf{start}}) = \boldsymbol{0}$. In the asymptotic region, the $\boldsymbol{C}^J(R_{\mathbf{end}})$ expressed in the molecular frame is transformed to that in the space fixed frame to deduce experimentally measurable quantities. These quantities are derived from the S-matrix evaluated by the following equation:

(I-4)

$$C^J_{jL\Omega\varepsilon}(R_{\mathrm{end}}) = \delta_{jj'}\delta_{LL'}\delta_{\Omega\Omega'}\delta_{\varepsilon\varepsilon'}\exp\left(-i\left(k_{j'\Omega'\varepsilon'}R - \frac{L'\pi}{2}\right)\right) - \left(\frac{k_{j'\Omega'\varepsilon'}}{k_{j\Omega\varepsilon}}\right)^{1/2} S^{(J)}_{j\Omega\varepsilon\to j'\Omega'\varepsilon'}\exp\left(i\left(k_{j\Omega\varepsilon}R - \frac{L\pi}{2}\right)\right)$$

where a wave vector $k_{j\Omega\varepsilon}$ is a function of the internal state. The scattering amplitude ($f_{jm\Omega\varepsilon\text{---}j'm'\Omega'\varepsilon'}$) is defined by;

$$f_{jm\Omega\varepsilon\to j'm'\Omega'\varepsilon'}(\hat{\boldsymbol{k}}') = \sum_{JLL'} i^{L-L'}[(2L+1)\pi]^{1/2}(2J+1)\begin{pmatrix} j & J & L \\ m & -m & 0\end{pmatrix}\begin{pmatrix} j' & J & L' \\ m' & -m & M_{L'}\end{pmatrix} (\delta_{jj'}\delta_{LL'}\delta_{\Omega\Omega'}\delta_{\varepsilon\varepsilon'} - S^{(J)}_{jL\Omega\varepsilon,j'L'\Omega'\varepsilon'})Y_{L'M_{L'}}(\hat{\boldsymbol{k}}) \tag{I-5}$$

and the SR-DCS is obtained by

$$\frac{\mathrm{d}\sigma_{jm\Omega\varepsilon\to j'm'\Omega'\varepsilon'}}{\mathrm{d}\omega}(\hat{\boldsymbol{k}}') = \frac{1}{k^2}\left|f_{jm\Omega\varepsilon\to j'm'\Omega'\varepsilon'}(\hat{\boldsymbol{k}}')\right|^2, \tag{I-6}$$

where $\hat{\boldsymbol{k}}$ and $\hat{\boldsymbol{k}}'$ are the initial and final collision wave vectors. The state-resolved integral cross section (SR-ICS) is given by,

$$\sigma_{j\Omega\varepsilon\to j'\Omega'\varepsilon'} = \frac{\pi}{(2J+1)k^2_{j\Omega\varepsilon}}\sum_J(2J+1)\sum_{LL'}\left|T^{(J)}_{jL\Omega\varepsilon,j'L'\Omega'\varepsilon'}\right|^2, \tag{I-7}$$

where the T-matrix is uniquely related to the S-matrix as

$$T^{(J)}_{jL\Omega\varepsilon,j'L'\Omega'\varepsilon'} = \delta_{jj'}\delta_{LL'}\delta_{\Omega\Omega'}\delta_{\varepsilon\varepsilon'} - S^{(J)}_{jL\Omega\varepsilon,j'L'\Omega'\varepsilon}. \tag{I-8}$$

The calculations can be simplified by introducing the following average and difference potentials constructed from the *ab initio* A′ and A″ potentials,

Published on 03 July 2002. Downloaded by Kyoto Daigaku on 09/09/2016 06:22:43.

View Article Online

$$V_{\mathrm{ave}}(R,\theta)=\frac{1}{2}(V_{\mathrm{A''}}(R,\theta)+(V_{\mathrm{A'}}(R,\theta))=\sum_{l}V_{l0}(R)d^{l}_{00}(\theta)$$
$$V_{\mathrm{diff}}(R,\theta)=\frac{1}{2}(V_{\mathrm{A''}}(R,\theta)-(V_{\mathrm{A'}}(R,\theta))=\sum_{l}V_{l2}(R)d^{l}_{20}(\theta) \qquad \text{(I-9)}$$

In the Hund's case (a) basis, the potential coupling term is expressed by the following equation where the fine structure conserving and changing transitions are determined by the average and difference potentials, respectively.

$$\left\langle j'L'\Omega'\varepsilon'J'M'\middle|V\middle|jL\Omega\varepsilon JM\right\rangle =$$

$$(-1)^{j+j'+J-\Omega}[(2j+1)(2j'+1)(2L+1)(2L'+1)]^{1/2}\sum_{l}\frac{1}{2}[1-\varepsilon\varepsilon'(-1)^{j+j'+l}]$$

$$\begin{pmatrix} L' & l & L \\ 0 & 0 & 0 \end{pmatrix}\begin{Bmatrix} j' & L' & J \\ L & j & l \end{Bmatrix}\left[\delta_{\Omega\Omega'}\begin{pmatrix} j' & l & j \\ -\Omega' & 0 & \Omega \end{pmatrix}V_{l0}(R)-\varepsilon(1-\delta_{\Omega\Omega'})\begin{pmatrix} j' & l & j \\ -\Omega' & 2 & -\Omega \end{pmatrix}V_{l2}(R)\right] \qquad \text{(I-10)}$$

Although full close-coupling calculations for RIS of open-shell systems are feasible with realistic PESs, calculations usually truncate the expansion for the vibrational coordinate r and reduce the dimensionality into two (the rigid rotor approximation). This approximation is still often employed and justified by a large ratio between an experimental collision energy and a vibrational frequency (the energy difference between $v = 0$ and 1 states). However, this restriction should be removed, as discussed by Tan *et al*. for the Al–H_2 bound state.[11] It may be worth mentioning the sudden approximations employed in the past: the explicit forms of these approximations were derived for open-shell systems by Alexander.[3] When a level spacing of a molecule was much smaller than the collision energy, the internal energy was replaced by an averaged value (the energy-sudden approximation). The coupled-state (centrifugal-sudden) approximation replaced the relative orbital angular momentum (L) by an average value ($\bar{L}$), which was sufficiently accurate for a short-range PES where a centrifugal term ($L^2/2\mu R^2$) was unimportant. The infinite-order sudden approximation that consists of both the centrifugal-sudden and energy-sudden approximations provided a simple form for SR-DCS.

(iii) General propensity rule

The interaction potential V in eqn. (I-1) arises from non-relativistic electrostatic interactions between a radical and a projectile. This means that the interaction matrix elements are diagonal for the electron and nuclear spin angular momenta. Electronic fine structures in a free radical are constructed by various angular momentum couplings, however, the spin-conserving propensity rule generally holds. For instance, in the case of the $^2\Pi_\Omega$ molecule in Hund's case (a), the projections of electronic angular momentum onto the molecular axis, Λ, and spin angular momentum, Σ, are good quantum numbers. The composite electronic angular momentum creates its

Published on 03 July 2002. Downloaded by Kyoto Daigaku on 09/09/2016 06:22:43.

View Article Online

Published on 03 July 2002. Downloaded by Kyoto Daigaku on 09/09/2016 06:22:43.

projection, $\Omega=|\Lambda + \Sigma|$, onto the axis. The inelastic scattering induces electronic transitions between the $^2\Pi_{1/2}$ and $^2\Pi_{3/2}$ states, and this efficiency is not strongly dependent on the atomic number of rare gas projectiles, for example. This is because electronic transitions are not induced by spin–orbit interactions but rather by electrostatic interactions that flip the orientation of Λ with respect to Σ, inducing the transition between the $\Omega = |\Lambda + \Sigma|$ and $|-\Lambda + \Sigma|$. In $^1\Pi$ systems, electrostatic interactions flip the direction of Λ, however, this results in the same electronic state $^1\Pi$ due to the lack of a spin angular momentum. As a result, RIS in the $^1\Pi$ state shows interesting quantum interference effects. It is noted that the origin of the fine structure changing transition in $^2\Pi$ and the interference effects in $^1\Pi$ have the same physical origin. That is why the earlier works on $^1\Pi$ molecules are valuable in understanding the $^2\Pi$ collision dynamics.

(iv) Incomplete list of SR-ICS and SR-DCS measurements

In Table 1 are summarized diatomic and linear radicals for which state-selective

Table 1 Rotational inelastic scattering of diatomic or linear free radicals studied by state-selective product detection

Collision system	Reference	Method
OH + H_2 (D_2)	92,93	XMB, LIF
OH($v = 1$) + H_2	92	IR pump–UV probe, cell, LIF
OH + *para*-, *normal*-H_2	97	XMB, hexapole, LIF
OH + He, Ar	85	XMB, hexapole, LIF
OH + Ar	82	XMB, hexapole, LIF
OH + CO, N_2, CO_2	90	XMB, hexapole, LIF
OH + CO, N_2	89	Rotatable XMB, LIF
OH($v = 2$) + He	87	IR pump–UV probe, cell, LIF
OH($v = 2$) + H_2O	88	IR pump–UV probe, cell, LIF
OH oriented beam[a]	143–145	Hexapole and static field, LIF
NCO + He, Ar	79,80,146,147	Rotatable XMB, LIF
CaCl + Ar	112	Beam-gas, quadrupole, LIF
CaCl + molecules[b]	8,113,114	Beam-gas, quadrupole, LIF
CaBr + Ar	6	Beam-gas, quadrupole, LIF
NO($v = 20$) + He	134	XMB, SEP, LIF
NO($v = 5$) + Ar	48	XMB, II
NO + Ar	130,131,135	XMB, LIF
Oriented NO + Ar	125–128	XMB, hexapole, LIF
NO($v = 3$) + He	148	IR pump–UV probe, cell, LIF
NO($v = 2$) + He, Ar, NO	149	IR pump–UV probe, cell, LIF
NO + Ar	23,24	Rotatable XMB, rotatable LIF
NO + Ar	42,43,45,46,139	XMB, II
NO + He, D_2	47	XMB, II
NO + diatomics[c]	137,138	Rotatable XMB, rotatable LIF
NO + He	38	Counterpropagating beam, REMPI-TOF
CH + D_2	150	Rotatable XMB, LIF
CH + He	78	Rotatable XMB, LIF
CN($v = 2$) + He, Ar	151,152	SEP, cell, LIF
NH + Ar	153	XMB, LIF

[a] Ar, CO, CO_2. [b] HCl, HCN, SO_2, NO, CH_3Cl. [c] NO, CO, O_2.

View Article Online

Published on 03 July 2002. Downloaded by Kyoto Daigaku on 09/09/2016 06:22:43.

integral and/or differential cross sections of RIS in the ground electronic state have been measured. Many of these have been already reviewed by others.[12–15] The laser-induced fluorescence (LIF) method prefers strongly fluorescent radicals such as OH, CH, CN, and NO. The NO radical can be easily ionized with a pulsed laser, so it has also been well studied by resonance enhanced multi-photon ionization (REMPI). Calcium halides (CaCl and CaBr) were studied using continuous wave (cw) lasers for their strong electronic transitions in the visible region and small rotational constants.

2 Measurements of SR-DCS

Spectroscopic selection of the final quantum states using tunable lasers is the unique approach used to measure SR-ICS and SR-DCS for free radicals with complex energy level structures. In laser-based detection, the LIF and REMPI methods are employed, where REMPI generally provides superior sensitivity to LIF. Note however that such a high sensitivity degrades under low vacuum in a static gas cell ($>10^{-4}$ Torr), where highly sensitive electron multipliers and microchannel plates are inapplicable.

Selection of the initial quantum state in crossed molecular beam (XMB) experiments is usually achieved by cooling the sample in a supersonic jet expansion. This limits the preparation of an initial state to the lowest state in energy. The Λ-doublet members are extremely close in energy, so its selection requires a sophisticated hexapole state selector. The hexapole also orients molecules. State-selective optical pumping, photoexcitation and stimulated emission pumping (SEP), to populate a single quantum state prior to collision have been performed in cell experiments, however, the application to beam experiments is quite limited so far.

Typical rotational energy level structures of free radicals are shown schematically in Fig. 1: more thorough descriptions of various internal level structures and optical selection rules are found in spectroscopy textbooks.[16–18] The frequency-resolution of pulsed dye lasers is usually 0.1 cm^{-1} that is sufficient to resolve rotational structures (characterized by a rotational B constant) in electronic transitions for most diatomic molecules consisting of the second-period elements. The spin–orbit splitting (characterized by a spin–orbit A_{SO} constant) in $^2\Pi$ electronic states varies from several to hundreds of cm^{-1}. The spin–orbit splitting separates the manifolds labeled by Ω ($= |\Sigma + \Lambda|$), in each of which the rotational ladder of $B(j + 1/2)^2$ ($B \ll A_{SO}$) is built up in Hund's case (a). The $^2\Sigma$ state has a simple rotational energy structure, $BN(N + 1)$, with a small splitting due to the spin–rotation interaction (characterized by a spin–rotation γ constant). This splitting is usually 10^{-3} cm^{-1} or less, and the Λ-doubling in the $^2\Pi$ state (characterized by p and q constants) is even smaller. The $^3\Sigma$ state has a spin–spin splitting (characterized by a spin–spin λ constant) of less than 1 cm^{-1}. When $\lambda \ll B$ (case (a)), a state with the rotational quantum number N splits into the three $j = N - 1$, N, $N + 1$ sublevels in the order of λ. The hyperfine structure of most cases except that of halogen-containing diatomics is too small to be resolved by a pulsed dye laser.

In what follows, we do not limit ourselves to open-shell systems but rather include experiments on closed-shell systems to overview the general techniques used to measure SR-DCS. Bergmann and co-workers combined an XMB apparatus with an LIF detector rotating around the scattering center,[19] as shown in Fig. 2(a). The scattered

View Article Online

Published on 03 July 2002. Downloaded by Kyoto Daigaku on 09/09/2016 06:22:43.

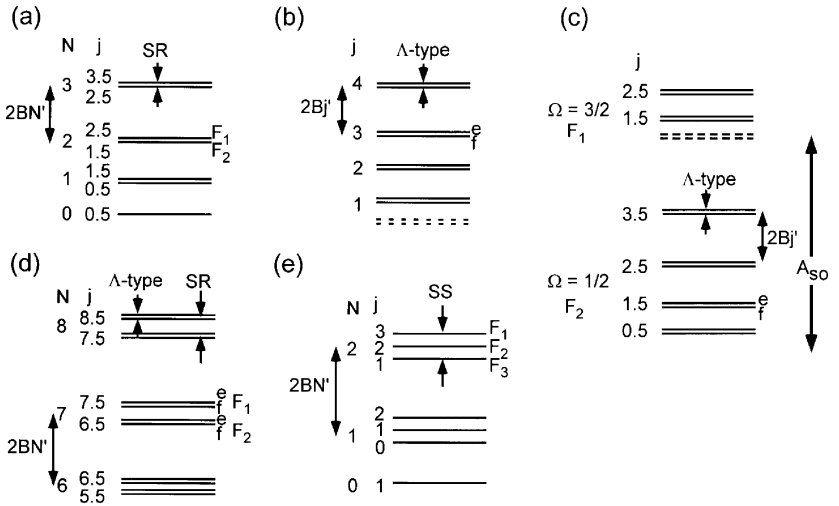

Fig. 1 Schematic energy level diagrams of open-shell diatomic molecules. The quantum numbers for rotational and total angular momenta are N and j, respectively. The approximate rotational level spacings, $2BN'$ or $2Bj'$, are indicated. The hyperfine structure is not shown. (a) $^2\Sigma^+$ electronic state. Each rotational state with N splits into the F_1/F_2 components by the spin–rotation (SR) interactions. (b) $^1\Pi$ electronic state. Each rotational state with j splits into two Λ-doublet states (*e*/*f*). (c) $^2\Pi$ electronic state in Hund's case (a). The spin–orbit manifolds, $\Omega = 1/2$ and $3/2$, are largely separated by A_{SO}. The rotational levels are designated by j, and each (j, Ω) state is split into the Λ-doublets (*e*/*f*). (d) $^2\Pi$ electronic state in Hund's case (b). Each rotational state with N splits into the F_1/F_2 components by the spin–rotation interactions and further into *e*/*f* states by the Λ-type doubling. (e) $^3\Sigma^+$ electronic state in Hund's case (a). Each rotational state with N splits into the $F_1/F_2/F_3$ components by spin–spin (SS) interactions.

product entering into the observation zone through the slit was detected by LIF using a single-mode cw dye laser (probe laser), yielding state-resolved scattering intensity as a function of the laboratory angle. This apparatus has been successfully applied to the vibrational and rotational inelastic scattering of $Na_2(^1\Sigma^+)$ with rare gas atoms.[20–22] Because of the small rotational constant of Na_2 (0.15 cm^{-1}) and the relatively high rotational temperature (~40 K) in the molecular beam, 30–40 initial levels were populated. Among these, the population of a particular initial state was modulated by the A $^1\Sigma_u^+$–X $^1\Sigma_g^+$ transition induced by another cw dye laser. The post-collision state of Na_2 was selectively observed by a probe laser also using the A–X band. State-to-state scattering intensity was obtained by taking the difference between the LIF intensities by toggling the target (rare gas) beam and the modulation laser beam.

Gentry, Giese and co-workers developed a sophisticated XMB apparatus with a differentially pumped LIF detector chamber,[23,24] as shown in Fig. 2(b). The initial state of the molecules was the lowest quantum state populated in a supersonic molecular beam. The scattered molecules entering through the slit into the detector chamber were probed by LIF using a detector with two spherical mirrors for enhanced sensitivity. Two molecular beam sources were rotated independently around the intersection point to achieve the collision energy of interest. The SR-DCSs were measured by

View Article Online

Published on 03 July 2002. Downloaded by Kyoto Daigaku on 09/09/2016 06:22:43.

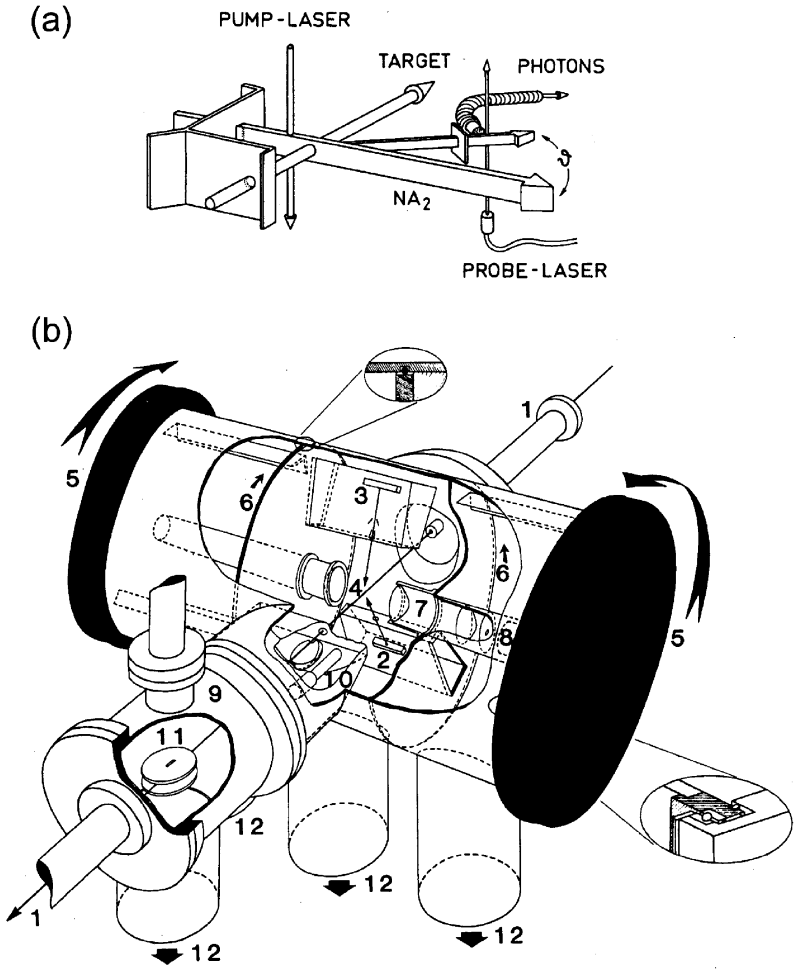

Fig. 2 The crossed molecular beam (XMB) apparatuses with LIF detectors. (a) The set-up employed by Bergmann and his co-workers. The optical pumping selected the initial state of Na_2. The scattered product was detected by the rotating LIF detector as a function of ϑ. (b) The XMB set-up developed by Gentry and co-workers. The components are (1) long light baffles, (2) and (3) pulsed molecular beam sources, (4) the beam crossing point, (5) separate rotating lids, (6) internal partition disks, (7) light-collection optics, (8) a photomultiplier tube, (9) a separate detector chamber, (10) the second LIF detector, (11) ion extraction optics, and (12) pumping ports. (9)–(11) are for the multiphoton ionization detection. Reproduced from ref. 19 for (a) and ref. 142 for (b).

rotating the two beam sources with respect to the detector while maintaining their intersection angle.[23]

A bolometer has sensitivity for vibrationally excited molecules. Keil and co-workers have employed the laser-bolometer detection of HF products in reactive[25,26] and inelastic scattering processes in the XMB.[27]

View Article Online

Published on 03 July 2002. Downloaded by Kyoto Daigaku on 09/09/2016 06:22:43.

Based on the fact that the Doppler shift ($\Delta\nu_D$) from a resonant absorption frequency (ν_R) is proportional to the velocity component ($v_{||}$) parallel to the direction of the laser propagation, appropriate analysis of a Doppler profile of the scattered products yields the SR-DCS.[28] Kinsey and Pritchard applied this method (ADDS: angular distributions using the Doppler shift) to measure the SR-DCS for the inelastic scattering of Na_2 + Ar.[29] ADDS has been also applied to reactive scattering.[30] A cw dye laser with a 1 MHz line-width is often employed to resolve the Doppler components, $\Delta\nu_D = v_{||}\nu_R/c$. For example, the Doppler shift for $v_{||}$=3000 m s^{-1} is about 5 GHz at 625 nm. Nesbitt and co-workers have used Doppler analysis in infrared laser absorption spectroscopy to explore the inelastic scattering in the XMB[31,32] and in a cell.[32]

Using the pump–probe scheme with two high-resolution ring dye lasers, McCaffery and his co-workers[33] performed measurements of velocity-dependent SR-DCS for RIS of alkali metal dimers in a cell. A narrow-band pump laser prepared a single quantum state and a particular velocity component of the molecules in an electronically excited state. The probe laser interrogated the post-collision state, and the SR-DCS was extracted from the Doppler profile in a subsequent electronic transition:[34] for example, Li_2 was excited to the A $^1\Sigma_u^+$ state and the post-collision state populated by RIS with Xe was probed by the A $^1\Sigma_u^+$–G $^1\Pi_g$ transition.[35] This velocity-selected double resonance (VSDR) method is applicable to inelastic scattering in an electronically excited state, while its variant, velocity-selected laser polarization spectroscopy (VSLP),[36] was used to study RIS in the ground electronic state.

Time-of-flight (TOF) mass spectrometry in conjunction with REMPI provides the velocity component parallel to the TOF axis, which is conceptually quite similar to laser Doppler spectroscopy. The advantages of the TOF method are the high sensitivity given by REMPI and the lack of requirement of an ultrahigh-resolution laser. Meyer used the counter-propagating XMB combined with a REMPI-TOF detection apparatus. The TOF axis was set parallel to the relative velocity vector (= counter-propagating molecular beam axis), so the signal intensities for different scattering angles appeared at different flight times (Fig. 3). With this method Meyer obtained the SR-DCSs for the RIS of NH_3 + Ar[37] and NO + He.[38]

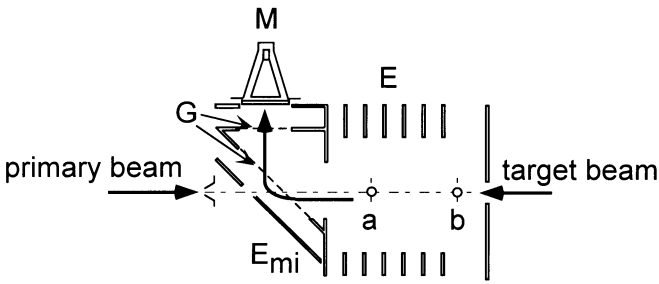

Fig. 3 The configuration of a counter-propagating XMB-TOF experiment by Meyer. M: microchannel plate detector, E: electrodes, E_{mi}: electrodes for an electrostatic mirror, G: grids (90% transmission), a, b: laser probing points. Reproduced from ref. 37.

View Article Online

Published on 03 July 2002. Downloaded by Kyoto Daigaku on 09/09/2016 06:22:43.

When a hydrogen atom is created as a product, almost all the translational energy is carried by the hydrogen atom due to its light mass, creating an extraordinary Doppler broadening. Liu and co-workers have combined Doppler spectroscopy and TOF measurements to obtain the DCS for F + H_2 reactive scattering in the XMB configuration.[39] A tunable laser propagating in the z-direction ionized the ensemble of H atoms with a particular v_z component, then these ions were extracted in the y-direction where the pinhole in front of the detector selected a particular value of v_x (core extraction). The resultant TOF spectrum reflected the v_y speed distribution for chosen v_x and v_z values. For hydrogen atoms, the Rydberg tagging method[40] is also used to obtain ultimate high-resolution in DCS measurements.

Since the first demonstration by Chandler and Houston,[41] the two-dimensional ion-imaging (II) method has been applied to various chemical dynamics experiments including bimolecular scattering, photodissociation, and photoionization. The method enables simultaneous measurements over all scattering angles, providing extremely accurate angular distribution, even for pulsed molecular beams and pulsed lasers with poor stabilities and the most efficient integration of the signal. Although only the 2D projection of an original 3D spatial scattering distribution is observed, angular information is well maintained in the projection. Ion-imaging coupled with the XMB method (Fig. 4) has been reported for inelastic,[42–48] and reactive scattering processes.[49,50]

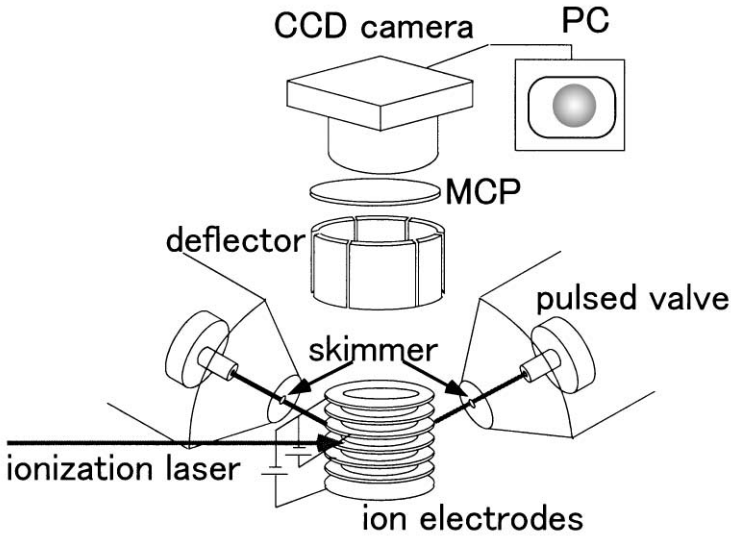

Fig. 4 Schematic diagram of the crossed-molecular beam ion-imaging apparatus. The two molecular beams generated by a pulsed valve cross inside ion acceleration electrodes. The scattered product is state-selectively ionized by a probe laser, and the ions are projected onto a microchannel plate (MCP). The velocity mapping ion optics provides spatial focusing, so the observed image only reflects the velocity component parallel to the detector face. The position of the ion appears as a light spot on a phosphor screen behind the MCP and is captured by a CCD camera.

View Article Online

Published on 03 July 2002. Downloaded by Kyoto Daigaku on 09/09/2016 06:22:43.

3 Extraction of SR-DCS in the XMB-II experiment

In photodissociation experiments, scattering distributions of neutral fragments exhibit cylindrical symmetry around the laser polarization. Likewise, scattering distributions in the XMB experiments have cylindrical symmetry around the relative velocity vector. Notice that these scattering distributions are defined by a *flux* given by the number density multiplied by the velocity of the products; the flux is the quantity conserved in the frame transformation between the center-of-mass (COM) and the laboratory (LAB) frame. In the actual experiments, measurements are performed in the laboratory frame using a laser beam that yields signal intensities proportional to the product densities. Therefore, care must be taken to consider properly the LAB velocity of the products in order to transform the observed results into the flux of particles correctly. In the RIS experiment, the velocity of the center of mass in the LAB frame and the recoil velocity of scattered particle are comparable, resulting in a LAB velocity strongly dependent on the azimuthal angle. As a result, the cylindrical symmetry that existed in the flux distribution of the neutral product is notoriously distorted in the observed ion image. Extensive and careful analysis is required to extract an accurate SR-DCS from the observed image.

Suppose that the pulsed molecular beams I and II, whose intensities are represented by $n_{\mathrm{I}}(\boldsymbol{R},t)$ and $n_{\mathrm{II}}(\boldsymbol{R},t)$ as a function of time t and the spatial position $\boldsymbol{R}$, are crossed in a vacuum chamber. The instantaneous scattering intensity is proportional to $n_{\mathrm{I}}(\boldsymbol{R},t)n_{\mathrm{II}}(\boldsymbol{R},t)$. Assuming that scattered particles generated at the time $-t$ and the position $\boldsymbol{R}$ move with the velocity in the laboratory frame $\boldsymbol{V}_{\mathrm{LAB}}$ until they are detected by the ionization laser light at $t = 0$ and the position $\boldsymbol{R}'$, where $\boldsymbol{R}' = \boldsymbol{R} + \boldsymbol{V}_{\mathrm{LAB}}t$. $\boldsymbol{V}_{\mathrm{LAB}}$ is a vector sum of $\boldsymbol{V}_{\mathrm{com}}$ (the center-of-mass velocity vector of the whole collision system) and $\boldsymbol{u}_{\mathrm{scat}}$ (the scattering velocity vector in the center-of-mass frame), $\boldsymbol{V}_{\mathrm{LAB}} = \boldsymbol{V}_{\mathrm{com}} + \boldsymbol{u}_{\mathrm{scat}}$. The center of the scattering distribution shifts in space by $\boldsymbol{V}_{\mathrm{com}}t$, and the radius of the distribution expands by $\boldsymbol{u}_{\mathrm{scat}}t$. The space-dependent detection efficiency, $f(\boldsymbol{R}')$, has boundaries given by the laser beam volume. Even if $\boldsymbol{u}_{\mathrm{scat}}$ has the same θ_{cm} with respect to the collision axis, the magnitude of $\boldsymbol{V}_{\mathrm{LAB}}$ will vary depending on the azimuthal angle as shown in Fig. 5: the density of the outgoing particle no longer has cylindrical symmetry around the axis. The particular side of an ion image where $\boldsymbol{u}_{\mathrm{scat}}$ and $\boldsymbol{V}_{\mathrm{com}}$ are anti-parallel to each other always exhibit more intensity than the opposite side where $\boldsymbol{u}_{\mathrm{scat}}$ is parallel to $\boldsymbol{V}_{\mathrm{com}}$.

Taking account of the $\boldsymbol{V}_{\mathrm{LAB}}$-dependent detection efficiency described above, a 2D image, $I(R_{\mathrm{image}},\theta_{\mathrm{image}})$, is generally represented by eqn. (III-1).

$$I(R_{\mathrm{image}},\theta_{\mathrm{image}}) = \tilde{P}_{2\mathrm{D}} \int_{-\infty}^{0} \mathrm{d}t \iiint \mathrm{d}\boldsymbol{R}' \left(n_{\mathrm{I}}(\boldsymbol{R},t) n_{\mathrm{II}}(\boldsymbol{R},t) f(\boldsymbol{R}') \frac{\mathrm{d}\sigma}{\mathrm{d}\omega}(\theta_{\mathrm{cm}}) \right), \qquad \text{(III-1)}$$

where $\tilde{P}_{2\mathrm{D}}$ denotes a 2D projection operator of a 3D object and $(\partial\sigma/\partial\omega)(\theta_{\mathrm{cm}})$ is the DCS. The relation of $\boldsymbol{R}' = \boldsymbol{R} + (\boldsymbol{V}_{\mathrm{com}} + \boldsymbol{u}_{\mathrm{scat}})t$, is implicitly included in eqn. (III-1). The equivalent formulae to eqn. (III-1) have been used by several groups for image analysis.[42,44,51]

View Article Online

Published on 03 July 2002. Downloaded by Kyoto Daigaku on 09/09/2016 06:22:43.

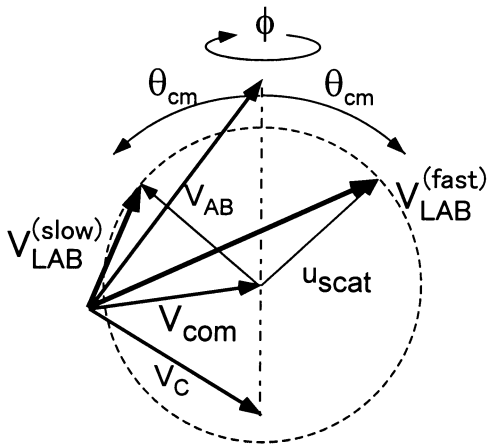

Fig. 5 The azimuthal angle dependent product velocity in the laboratory frame. The two molecular beams with velocities V_{AB} and V_C define the collision axis indicated by a broken line, from which the center-of-mass scattering angle (θ_{cm}) is measured. The scattering distribution of state-selected AB product will have the same speed in the center-of-mass frame and appear on the dotted circle (Newton circle). When the recoil velocity in the center-of-mass frame, $\boldsymbol{u}_{scat}$, is added to the velocity of the center of mass, V_{com}, the composite velocity largely varies with the mutual angle between these vectors. This results in the azimuthal angle (ϕ) dependence of the product number density and asymmetric ion image.

The velocity spread of molecular beams, which leads to the collision energy spread ($\Delta\varepsilon_{coll}$) and blurring of the Newton diagram ($\Delta\theta_{cm}$) as described later, can be included in n_I and n_{II} as

$$n(R,t) = \int_{-\infty}^{\infty} g(v)u(v,R,t)\mathrm{d}v, \qquad \text{(III-2)}$$

where $u(v,R,t)$ represents an ensemble of molecules with a single speed of v, and $g(v)$ is the coefficient. The collision energy spread and blurring of the Newton diagram may also be taken into account phenomenologically by blurring the $I(R_{image},\theta_{image})$ determined for a single collision energy (ε_{coll}) with appropriate coefficients for $\Delta\varepsilon_{coll}$ and $\Delta\theta_{cm}$, under the assumption that the DCS and the V_{LAB}-dependent detection efficiencies do not vary. The former and the latter convolution may be performed by

$$\int_0^{\infty} \mathrm{d}\alpha\, g(\alpha)[\hat{T}(\alpha)I(R_{image},\theta_{image})] \qquad \text{(III-3)}$$

and

$$\int_0^{2\pi} \mathrm{d}(\Delta\theta)g(\Delta\theta)[\hat{U}(\Delta\theta)I(R_{image},\theta_{image})], \qquad \text{(III-4)}$$

View Article Online

with the operator $\hat{T}(a)$ magnifying the 2D image a times, and the operator $\hat{U}(\Delta\theta)$ rotating the 2D image by $\Delta\theta$ degrees, where g denotes a weight-function.

Once the parameters in eqn. (III-1) are obtained, the DCS is extracted by minimizing the difference between an observed image and a simulated result. The least-squares fitting of 2D images is straightforward when the basis functions are introduced to describe the DCS.[51] The fitting of a 1D distribution such as the intensity around a selected radius on an image,[42] or the projection onto the collision axis is even simpler.[44]

Published on 03 July 2002. Downloaded by Kyoto Daigaku on 09/09/2016 06:22:43.

4 Angular resolution in the XMB-II method

Spatial resolution of ion-imaging has been improved dramatically by the velocity mapping method introduced by Eppink and Parker.[52] This configuration of an ion optics, an immersion lens, focuses the ions having the same velocity component into a single spot on the imaging detector, completely removing the blurring due to non-negligible ionization volume. On the other hand, even if a single ion hits the detector, the resulting light spot spreads over several pixels on the CCD chip, which degrades an imaging resolution. This blurring must be corrected by image capturing software[53,54] that calculates the center of gravity for each light spot in every video frame. The software also corrects uneven detector sensitivity over the area of an imager.

The velocity mapping and centroiding algorithm are essential for obtaining high-resolution in imaging of photofragments and photoelectrons. On the other hand, angular and velocity resolutions in the XMB experiments are restricted not only by an imaging resolution but also by unavoidable velocity spreads of molecular beams. The spread of the relative velocity (Δv_{rel}) is directly transformed into the collision energy spread ($\Delta\varepsilon_{coll} = \mu v_{rel}\Delta v_{rel}$) and the spread of scattering velocity ($\Delta v_{scat} \propto (v_{rel}/v_{scat})\Delta v_{rel}$), where μ is the reduced mass of a collision system. Thus, the product velocity distribution is inevitably blurred by this effect. The SR-DCS at a single collision energy (ε_{coll}) without energy spread ($\Delta\varepsilon_{coll} = 0$) is expected to show fine oscillation with a period of the order of one degree in the forward direction. The phase of this rapid oscillation varies sensitively with ε_{coll}, and this feature is easily washed out for incomplete control of the collision energy.

The velocity-spread of the molecular beams also reduces the angular resolution. As shown in Fig. 6, the small change in the beam velocity rotates the relative velocity vector in the collision plane, blurring the angular distribution: for example, two molecular beams with the same mean velocity and 10% spread crossed at right angles lead to the rotation of the relative velocity vector by as much as ±6 degrees in the collision plane.

5 Classical mechanical model of the rotational rainbow

The rotational rainbow (RR)[55,56] is often inferred in RIS. This concept is phenomenologically analogous to a well known rainbow effect in atom–atom elastic scattering. In the classical mechanical description of atom–atom scattering, there is a unique relation between the impact parameter b and the deflection angle χ. Due to the

View Article Online

Published on 03 July 2002. Downloaded by Kyoto Daigaku on 09/09/2016 06:22:43.

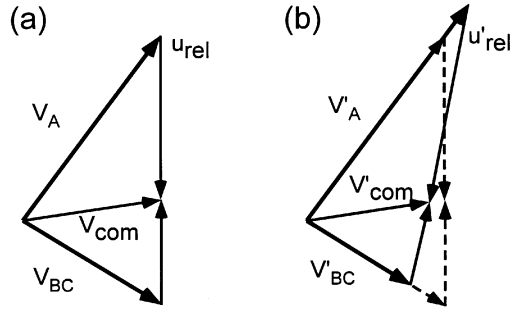

Fig. 6 The comparison of the Newton diagrams between (a) particular velocities of $\boldsymbol{V}_{AB}$ and $\boldsymbol{V}_C$, and (b) slightly modified $\boldsymbol{V}'_{AB}$ and $\boldsymbol{V}'_C$. The velocities of the center of mass are designated by $\boldsymbol{V}_{com}$. $\boldsymbol{u}_{rel}$ indicates the axis of relative velocity (collision axis). It is seen that the collision axis is rotated clockwise for this particular change of the beam velocities.

presence of the attractive and repulsive parts of the potential, the extremum occurs in the deflection function, $\chi(b)$, which leads to a singularity in the differential cross section (a classical rainbow). In the case of atom–diatom scattering, the alignment angle γ with respect to the relative velocity vector is added as another degree of freedom. Therefore, the extrema of the Jacobian determinant of the partial derivative of the two initial variables, b and γ, with respect to the final observable, θ and j, need to be considered. The singularities originating from these extrema are termed as the rotational rainbow or rainbow peaks, however, they occur even for a purely repulsive atom–diatom potential in contrast with the atom–atom rainbow.

When the collision energy is considerably larger than the well depth of the potential, RIS may be predominantly induced by the repulsive wall of the potential. The hard-sphere model approximates the repulsive wall by an infinitely high step function. In the case of a diatomic molecule, the anisotropy of the repulsive wall can be generally truncated at the V_2 ($l = 2$) term, which results in an ellipsoidal shape. The hard-ellipsoid model proposed by Bosanac[57] (Fig. 7) is characterized by three potential parameters A (major axis), B (minor axis), and δ (the distance between the center of the ellipsoid and the center of gravity in the case of a heteronuclear diatomic molecule). Classical trajectories are calculated with the two parameters b (impact parameter) and γ (incident direction to the ellipsoid with respect to the relative velocity vector) in the case of a non-rotating diatomic molecule, and the SR-DCSs are obtained from the resultant trajecteries as a function of both the scattering angle (θ) and the classical rotational excitation j. Clearly, a rotational rainbow originates from the anisotropy of the potential. Calculations have illustrated a rotational rainbow for a homonuclear molecule, a double rainbow for a heteronuclear diatomic molecule due to collisions at the different ends,[58] and multiple collisions[59,60] due to chattering of a rotating molecule with a projectile.

McCaffery proposed the angular momentum model[61,62] and a path integral approach[63] to RIS. In the angular momentum model, rotational excitation is attributed to an impulsive conversion of the (translational) linear momentum to the (rotational) angular momentum, similar to Bosanac's hard-ellipsoid model. The most probable scattering angle (θ_p) for a particular rotational excitation (Δj) is related to the

View Article Online

Published on 03 July 2002. Downloaded by Kyoto Daigaku on 09/09/2016 06:22:43.

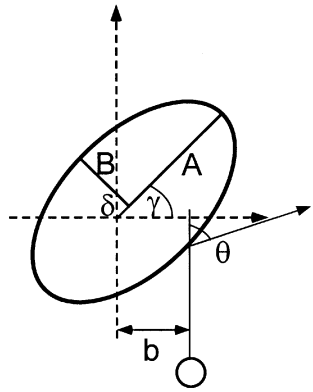

Fig. 7 A hard-ellipsoid model by Bosanac. The atom–diatom interaction potential surface is approximated as the ellipsoidal boundary, whose major and minor axes are A and B. The distance between the center of gravity and the center of the ellipsoid of a heteronuclear diatomic molecule is designated by δ. An incoming atom with impact parameter b and relative angle γ is impulsively reflected at the ellipsoidal boundary into the scattering angle (θ).

incident relative velocity (v_i) and threshold velocity (v_{th}) to open the Δj channel by $\sin(\theta_p) = v_{th}/v_i$. The calculated Δj-dependence of θ_p is in fair agreement with the experimental results on Li_2 + Rg[64] and Na_2 + Rg.[62]

Molecular alignment in RIS has been treated by the geometric[65] and kinematic[66–68] apse models. The path integral[63] and Fraunhofer approximation[69] have been employed to analyze a fast oscillation in the SR-DCS due to quantum mechanical interference. Calculations using the path integral method and the infinite-order-sudden approximation were compared for the N_2 + Rg and Na_2 + Rg systems,[63] and consistent results were obtained. The Fraunhofer approximation was employed to analyze the SR-DCS for the RIS of CH_4 + He and N_2 + He.[69]

Notice that these models essentially consider the effect of mechanical torque on a closed-shell molecule, and they are unable to describe coherent dynamics that induces fine structure transitions and various interference effects in open-shell systems. Nevertheless, the models may be useful for interpreting the fine-structure conserving process in the RIS of free radicals.

When we consider a realistic PES with an attractive and a repulsive part, the relation between the topography of the PES and the scattering amplitudes should be examined. Trajectory surface-hopping calculations would be one of the simplest approaches, however, this has not been examined extensively. Alexander has performed such calculations using *ab initio* PESs[70,71] to obtain SR-ICS in both $\Delta\Omega = 0$ and $\Delta\Omega = 1$ transitions in the CN(A $^2\Pi$) + He scattering.[72] The result was in reasonable agreement with coupled-state calculations using the same PESs.

Connor and his co-workers have applied the nearside–farside (NF) approach, originally developed for nuclear heavy-ion scattering, to RIS. This method decomposes the scattering amplitude, $f_{i\longrightarrow f}(\theta_{cm})$, into the nearside component ($f^{N}_{i\longrightarrow f}(\theta_{cm})$) and the farside ($f^{F}_{i\longrightarrow f}(\theta_{cm})$) component that are essentially the trajectories mainly through the repulsive core and the long-range attractive region, respectively.[73,74] The input quantities in the NF method are semi-classical or quantum

View Article Online

Published on 03 July 2002. Downloaded by Kyoto Daigaku on 09/09/2016 06:22:43.

scattering matrix elements expanded by partial waves. In the applications to the HF + Ar[74] and N_2 + Ar[75] RIS, the backward scattering was dominated by the nearside amplitude while high-frequency oscillations occur at small θ_{cm} by interference between the nearside and farside, as expected. The NF decomposition has also been applied to the reactive scattering of F + H_2, H + D_2 (ref. 76) and I+HI.[77]

6 Case studies

Here, we overview several examples with a focus on the state-specificity in RIS.

(i) Case (a) *vs.* case (b); NCO + He and CH + He

Macdonald and Liu carried out XMB SR-ICS measurements for RIS of two representative $^2\Pi$ radicals, CH ($X\ ^2\Pi_i$) and NCO ($X\ ^2\Pi_r$), with He.[78–80] The rotational level spacings in the CH radical with a large B constant of 14.2 cm^{-1} are much larger than the spin–orbit energy A_{SO} = 28.1 cm^{-1} (Hund's case (b)). Each rotational level with a nuclear rotational quantum number N is split by the spin–rotation interactions into the fine structure levels of F_1 ($j = N + 1/2$) and F_2 ($j = N - 1/2$). Each of the F_1 and F_2 components splits further into the Λ-doublet, resulting in a quintet. Macdonald and Liu measured the SR-ICS at various collision energies by using rotatable molecular beam sources. Using the optical selection rules of $\Delta j = 0,\pm1$ and of the total parity $(+)\longrightarrow(-)$, $(-)\longrightarrow(+)$, all four F_1/F_2 and *e*/*f* fine structure sublevels associating with the same N rotational state were resolved in the LIF detection using the $A\ ^2\Delta$–$X\ ^2\Pi$ band. The collision induced transition probability into the fine structures (FSP in their designation) from the equally populated *e*/*f* initial states exhibited a strong preference for the F_1–*f* and F_2–*e* final states having a common reflection symmetry of $\Pi(A'')$ (Fig. 8(a)). This preference persisted over the collision energy, by a factor of 3–4, where subgroups with the same $\Pi(A')$ or $\Pi(A'')$ symmetry behaved similarly. The preference for the Λ-doublet in case (b) while it is absent in case (a) is explained in terms of the matrix element in the close-coupling calculations in the case (b) basis;[81] the preferential population in the $\Pi(A'')$ components was predicted for the $^2\Pi$ radical with π^3 occupancy such as OH ($X\ ^2\Pi_i$), while the observed $\Pi(A')$ preference for the CH ($X\ ^2\Pi_r$) radical is explained by its π^1 occupancy.

The NCO radical with A_{SO} of -95.6 cm^{-1} and B of 0.39 cm^{-1} in the ground vibronic state belongs to Hund's case (a). The SR-ICS measurements provided the Δj distributions that are dramatically different for the spin–orbit conserving ($\Delta\Omega = 0$) and changing ($\Delta\Omega = 1$) transitions:[79,80] the $\Delta\Omega = 0$ transition (Ω''=3/2 $\longrightarrow$ Ω'=3/2) rapidly decreased as Δj increased, while a bell-shaped Δj distribution was observed for the $\Delta\Omega = 1$ (Ω=3/2 $\longrightarrow$ Ω'=1/2) transition (Fig. 8(b)). The contour of the sum potential resembled an ellipsoid, from which the monotonically decreasing Δj distribution in the $\Delta\Omega = 0$ transitions was explained by analogy with the $^1\Sigma$-diatom collisions. On the other hand, the difference potential was short-ranged and much more anisotropic in nature, so the bell-shaped distribution in the $\Delta\Omega = 1$ transition was attributed to the trajectories with small impact parameters that would not lead to small Δj transitions.

View Article Online

Published on 03 July 2002. Downloaded by Kyoto Daigaku on 09/09/2016 06:22:43.

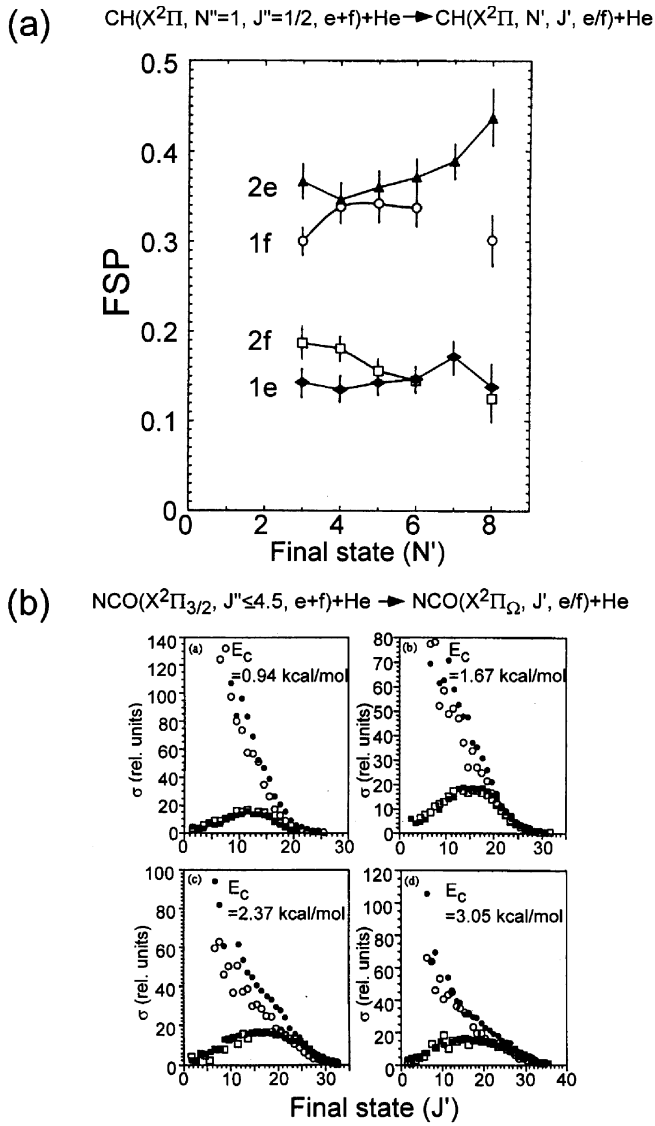

Fig. 8 State-resolved integral cross sections in RIS of CH + He and NCO + He. (a) The fine-structure probability (FSP = $\sigma(N',F_i,e/f)/\Sigma_{F_i,e/f}\sigma(N',F_i,e/f)$) for CH($N''$=1) + He ⟶ CH($N'$) + He. The connecting lines are only to clarify the trend. The error bars are $\pm 2\sigma$ due to uncertainty from seven to nine measurements. The preferential population of the Π(A″), 2*e* and 1*f*, *Λ*-doublet state is clearly evident. (b) The relative state-resolved integral cross sections NCO($^2\Pi_{3/2}$, $J'' \leqslant 4.5$, $e + f$) + He ⟶ NCO($^2\Pi_{3/2,\ 1/2}$, J', e/f) + He at four collision energies. Each symbol represents the product state: ●, $^2\Pi_{3/2}(f)$; ○, $^2\Pi_{3/2}(e)$; ■, $^2\Pi_{1/2}(f)$; □, $^2\Pi_{1/2}(e)$. At all collision energies, the spin–orbit conserving process exhibits a monotonically declining cross section for *j* while bell-shaped distributions are confirmed for the spin–orbit changing process. Reproduced from ref. 78 for (a) and ref. 80 for (b).

View Article Online

Published on 03 July 2002. Downloaded by Kyoto Daigaku on 09/09/2016 06:22:43.

(ii) Preferential Λ-doublet population; OH + He and OH + H_2

The inelastic scattering of the OH ($X\ ^2\Pi_i$) radical is important in combustion chemistry, atmospheric chemistry, and astrochemistry. The interstellar OH maser action has been speculated to be due to the population inversion induced by RIS with H_2 in the space. Most recently, ter Meulen and his co-workers measured the SR-ICS for the inelastic scattering of OH + Ar at the collision energy of 746 cm^{-1} by using the XMB-LIF method.[82] They used a double-hexapole state selector to choose the single *f*-state $j = 3/2$, $\Omega = 3/2$ as an initial state for RIS with OH. The RIS was dominated by small Δj spin–orbit conserving transitions. Close-coupling calculations using the CEPA (correlated electron pair approximation[83]) and UMP4 (unrestricted fourth-order Møller-Plesset perturbation theory[84]) for *ab initio* PESs reproduced the general trends, where the latter showed superior agreement with the experimental result. The RIS of OH with He has also been investigated experimentally[85] and theoretically.[86]

One of the most important observations was the preferential *Λ*-doublet population in RIS, especially the preference of the *e*-state in the spin–orbit conserving transition. This propensity was explained in terms of quantum interference. Briefly, the potential coupling matrix element in the case (b) can be expressed by $A^1_{i,j}V_{l0}(R) + B^1_{i,j}V_{l2}(R)$ where the coefficients *A* and *B* vary with the internal state of OH (as indicated by the running indices of *i* and *j*). The relative signs of *A* and *B* are opposite for the Π(A′) but identical for the Π(A″) final states. The $\Omega = 3/2(f)$ and the $\Omega = 1/2(e)$ states are both Π(A″), while $\Omega = 3/2(e)$ and $\Omega = 1/2(f)$ are Π(A′). As expected from the π^3 occupancy,[81] the two sets of *ab initio* calculations showed that both the $V_{l0}(R)$ (average PES) and $V_{l2}(R)$ (difference PES) terms were predominantly positive: the difference between the π^3 and π^1 occupancy is that the A″ electronic state of the former directs the lone-pair electrons towards the projectile while the latter directs a vacant orbital, resulting in opposite ordering of the A′ and A″ states in energy. Therefore, the case where *A* and *B* have identical sign gains the intensity, resulting in preference for the final Π(A″) states, while the intensities of the Π(A′) final states diminish. The "interference" accounts generally for the unequal population in the *Λ*-doublet in any case (b) radicals.

Similar preferential populations in the *Λ*-doublet have been reported for the RIS of OH with He,[87] H_2, H_2O,[88] N_2, CO, and CO_2.[89,90] Among them, the works on OH + H_2 have direct implications to the interstellar OH maser action.[91] Andresen and his co-workers observed the preferential population of the Π(A′) components both in the $\Omega = 1/2$ and 3/2 states by their XMB-LIF method on OH + *normal*-H_2,[92,93] where the initial state was the mixture of the Π(A′) and Π(A″) doublet in the lowest $j'' = 3/2$, $\Omega'' = 3/2$ state. The ratio of the SR-ICS for the Π(A′) to Π(A″) final states in the same (j',Ω') increased with Δj. Population inversion was observed among the *Λ*-doublet in the $\Omega = 1/2$ manifold, but not in the $\Omega = 3/2$ manifold. Calculations[94,95] using *ab initio* PESs[96] reproduced these features qualitatively. On the other hand, Schreel and ter Meulen performed similar measurements of the SR-ICS for OH + H_2 at the collision energy of 595 cm^{-1},[97] in which the hexapole state selector prepared almost a pure single *e*-state with $j'' = 3/2$ and $\Omega'' = 3/2$. The ICSs were measured for both *para*-H_2 ($j(H_2) = 0$) and *normal*-H_2 (3:1 mixture of *ortho*-H_2 ($j(H_2) = 1$) and *para*-H_2 ($j(H_2) = 0$)) and compared with close-coupling calculations[98] using *ab initio* PESs by Offer and

View Article Online

Published on 03 July 2002. Downloaded by Kyoto Daigaku on 09/09/2016 06:22:43.

Vanhemert.[99] Fair agreement was observed between the experimental and theoretical results. Although the population inversion in the Λ-doublet in the $j' = 1/2$, $\Omega' = 1/2$ was seen in the collision with *para*-H_2 both experimentally and computationally, such an inversion disappeared with *normal*-H_2 as a projectile and with the equally populated Λ-doublet $j'' = 3/2$, $\Omega'' = 3/2$ state as an initial state for RIS. This implied that the RIS with H_2 may not be responsible for the population inversion leading to the interstellar OH maser action. Note, however, that this may be concluded only after thorough consideration is given to the astronomical environment such as collision energy, initial state distribution, and radiation field.

(iii) Alkali-metal dimer in the electronic excited $^1\Pi$ state

In the early 1970s, pioneering SR-ICS measurements were carried out for RIS within the $^1\Pi$ electronically excited state of alkali-metal dimers. Some of these RISs in electronically excited states have been reviewed by Dagdigian.[100] These works are important in that knowledge of the $^1\Pi$ system paves the way to understanding the dynamics of $^2\Pi$ radicals. Ottinger *et al.* excited Li_2 to the B $^1\Pi_u$ state in a gas cell filled with Ar using multiple lines of an Ar^+ laser (around 500 nm) and obtained the SR-ICS from the dispersed fluorescence spectrum.[101] The same technique was applied to the RIS of Na_2 ($B^1\Pi$)[102,103] and NaLi ($^1\Pi$)[104] with rare gas atoms and molecules. One of the most important results from these experiments was the asymmetry of ICS for the $\pm\Delta j$ processes which depended on the Λ-doublet (these were termed the *c*- and *d*-components at that time). In the case of Li_2 + Ar, $c \longrightarrow c$ and $d \longrightarrow d$ transitions exhibited equal intensities for $+\Delta j$ and $-\Delta j$, while, the $c \longrightarrow d$ transition favored $-\Delta j$ over $+\Delta j$ and the $d \longrightarrow c$ the opposite. The degree of $\pm\Delta j$ asymmetry varied with collision partners, however all showed similar trends. The *c*/*d* labeling corresponds to the more modern *e*/*f* labeling.

The observed asymmetry of the $\pm\Delta j$ transitions was related to the different electronic distribution in these Λ-doublet states: the electronic charge distributions in the *c*- and *d*-components are $\cos^2\phi$ and $\sin^2\phi$, where ϕ is the azimuthal angle about the internuclear axis. The ϕ-dependent interaction potential, that was intuitively introduced, explains the asymmetry.[105–107] The introduction of the ϕ-dependent interaction potential was obviated later, and the adiabatic PES obtained by an *ab initio* method were employed in the calculations.[7,108]

Alexander and Dagdigian clarified the symmetry properties of the Λ-doublet in the $^{1,2,3}\Pi$ states with respect to the plane of rotation.[109] The new nomenclature, $\Pi(A')$ and $\Pi(A'')$ for the Λ-doublet, is more relevant to the collision dynamics[110] than the spectroscopic *e*/*f* labeling.[111] Note that this $\Pi(A'')$ (or $\Pi(A')$) symmetry designates the reflection symmetry of the unpaired electron orbital through the molecular rotation plane which should be discriminated from the reflection symmetry of a triatomic system through the molecular plane. It was shown that a single Λ-doublet (*e* or *f*) state of the $^{1,2,3}\Pi$ state belongs to the $\Pi(A')$ or $\Pi(A'')$ symmetry in the case (b) (high-*j*) limit, while in the case (a) limit, none of the *e*/*f* components of the $^2\Pi$ state have definite $\Pi(A')$ or $\Pi(A'')$ symmetry.

View Article Online

Published on 03 July 2002. Downloaded by Kyoto Daigaku on 09/09/2016 06:22:43.

(iv) Propensity for the spin-doublet in the $^2\Sigma$ state; CaX (X = Cl, Br) + Ar

Dagdigian and his co-workers carried out beam-gas scattering experiments of highly polar open-shell radicals, CaCl ($X\ ^2\Sigma^+$) and CaBr ($X\ ^2\Sigma^+$) with Ar.[6,112] These were extended to the scattering with polar collision partners,[8,113,114] where the dipole–dipole interactions dominate the intermolecular potentials. The energy level structure of CaX is Hund's case (b). The second-order Stark effect with a large electric dipole moment of CaCl (μ_e = 4.3 D) allowed state-selective beam deflection and refocusing using a quadrupole state selector, which successfully confined the initial state of CaCl to be $N = 2$ (e, or F_1, $j = 5/2$). The typical ambient pressure of Ar in the collision cell was 10^{-4} Torr. The post-collision state was detected by LIF using a cw ring dye laser. A strong propensity was observed for the *e*/*f* conserving transition, which is reproduced by calculations based on the electron gas model.[115] The calculations of the nuclear dynamics employed the sudden limit scaling, which relates the $\sigma_{(N'',j'')\longrightarrow(N',j')}$ to the j-independent cross section σ_j, and the recoupling scheme introduced by Corey and McCourt.[116] This reduced the computation time by relating the cross sections of the $^2\Sigma$ molecules to those of $^1\Sigma$. The propensity of the *e*/*f* conservation was essentially due to the inability of the electrostatic interaction to affect the orientation of $\boldsymbol{S}$ with respect to $\boldsymbol{N}$. In CaBr + Ar, the hyperfine component due to the nuclear spin ($\boldsymbol{I}$) of Br (I = 3/2) of CaBr was selected by the quadrupole state selector as the initial state of collision.[117] After the collision with Ar, the hyperfine component in CaBr was interrogated by a high-resolution dye laser, which elucidated the hyperfine propensity of $\Delta F = \Delta j$. The physics behind this recoupling is that the nuclear spin $\boldsymbol{I}$ is unchanged by the collision.

(v) SR-DCS in NO + Ar

Nitric oxide + Ar (rare gas atom) is the most intensively studied among the RIS of free radicals. Nitric oxide in the ground state ($^2\Pi_r$) has the spin–orbit constant A_{SO} = 123.1 cm^{-1} and the rotational constant B = 1.7 cm^{-1}. As the rotational energy becomes comparable with the spin–orbit energy, the coupling case gradually changes from Hund's case (a) to (b), while the symmetry notation in the case (a) basis is used throughout. The equilibrium structure of the NO–Ar complex has been determined to be a T-shape by Howard and his co-workers using microwave spectroscopy and molecular beam electric resonance.[118,119] The binding energy of the complex is D_0 = 87.8 cm^{-1} as determined by Tsuji *et al.* using electronic spectroscopy,[120] and IR spectroscopy of the NO stretch in the complex was performed by Meyer's group[121] (NO–Ne[122]). One of the earliest XMB experiments by Thuis *et al.*[123,124] measured the orientation-dependent ICS using a hexapole and correctly predicted the T-shaped equilibrium geometry without any spectroscopic means. Stolte's group has been providing valuable and unique experimental results using the oriented NO beam since then.[125–128] Casavecchia *et al.* obtained a similar anisotropy of the interaction potential from the (state-unresolved) DCS using XMB equipped with a universal detector.[129]

Andresen and his co-workers observed the SR-ICS for NO + Ar (also with other rare gas atoms) by XMB-LIF[130,131] at a collision energy of 444 cm^{-1}. The observed

View Article Online

Published on 03 July 2002. Downloaded by Kyoto Daigaku on 09/09/2016 06:22:43.

$\Delta\Omega = 0$ ICS decreased monotonically with Δj, while a bell-shaped Δj distribution was found for the $\Delta\Omega = 1$ transition. Both the $\Delta\Omega = 0$ and 1 SR-ICSs exhibited alternation for even and odd Δj processes. These features were reproduced by calculations using the coupled-state approximation and the electron gas model PESs, although the theoretical cross section for the $\Delta\Omega = 1$ was smaller than the observed value by a factor of ~4.[132] The even–odd alternation observed in the $\Delta\Omega = 0$ transition was explained by the dominant $l = 2$ term consisting of the average potential (V_{ave}). Bieler *et al.* observed the SR-ICS of the NO collision with Ar, Xe, CO, N_2, O_2, N_2O, and CO_2,[133] where the collision energies for the particular case of Ar are 500 cm^{-1} and 2250 cm^{-1}. Drabbels *et al.* studied RIS of the highly vibrationally excited NO (v_{NO} = 20) with He by stimulated emission pumping.[134] Although the collision energy was only 195 cm^{-1}, the total energy (= initial internal energy + collision energy) was considerably higher than in other experiments. The observed SR-ICS for the $\Delta\Omega = 0$ and $\Delta\Omega = 1$ RIS were compared with the close-coupling calculations using an *ab initio* PES and a rigid rotor approximation, and good agreement with the experimental result was obtained. The SR-ICS of the NO + Ar was also more recently measured by Lin *et al.* at the collision energy of 1774 cm^{-1}.[135] Again, the monotonic decrease and the bell-shaped Δj distribution were observed for the $\Delta\Omega = 0$ and 1 transitions, respectively.[79] The Λ-doublet preference in the $\Pi(A'')$ component in the higher Δj transition is observed in both the $\Delta\Omega = 0$ and 1 transitions, which is consistent with the gradual change from the case (a) to (b) as j increases: the preference by a factor of ~ 1.5, also observed by Bieler *et al.* at the collision energy of 2250 cm^{-1}, was much weaker than in the $^2\Pi$ case (b) radicals, CH and OH. The coupled-state scattering calculations based on *ab initio* PESs reproduced the $\Pi(A'')$ preference in the higher Δj transitions, although the $\Delta\Omega = 1$ ICS was underestimated by a factor of ~2.[136]

In the last decade, pioneering SR-DCS measurements for the NO + Ar system were carried out by Gentry's group[23,24] and Houston's group[45,46] by different approaches. Gentry and his co-workers took a conventional LIF approach, while their unique rotatable beam sources were utilized to change collision energies from 117 to 1694 cm^{-1}. This apparatus has also been applied to NO + other diatomic colliders.[137,138] The collision kinematics and the beam velocity spread made their angular resolution worse than 9 degrees. The DCS observed for a limited θ_{cm} range and the final states (j' = 1.5, 2.5, 8.5, 12.5, 14.5, Ω' = 1/2) exhibited the moderate tendency of a scattering maximum gradually shifting from the forward to the backward direction as Δj increases.[56] Agreement with close-coupling calculations using the CEPA PESs was fair.[136] At the higher collision energy of 1695 cm^{-1}, the angular distribution for the j' = 18.5, Ω' =1/2 final state manifested two peaks, which were regarded as a "double rainbow" corresponding to a classical hard-sphere collision at the two ends of the heteronuclear diatomic molecules.[58]

Houston and his co-workers employed a novel ion-imaging approach,[45,46] and measured the SR-DCSs at three collision energies of 887, 1452, and 3145 cm^{-1} for the $\Delta\Omega = 0$, and, for the first time, the $\Delta\Omega = 1$ transition. Scattering into the entire θ_{cm} (= 0–π) range is simultaneously observed, which provides a relatively *short* integration time to determine the SR-DCS, 4 h for the $\Delta\Omega = 0$ transition and 10–12 h for the $\Delta\Omega = 1$ transition. The experimental angular resolution was estimated to be 8 degrees. A Monte Carlo forward convolution program considering numerous trajectories of NO in the vacuum chamber was employed to simulate the observed

View Article Online

Published on 03 July 2002. Downloaded by Kyoto Daigaku on 09/09/2016 06:22:43.

images. In the $\Delta\Omega = 0$ transitions, the strong forward peak observed for $j' = 7.5$ has shifted to a larger θ_{cm} angle as j' increases, and a double peak appears at $j' = 18.5$. These peaks were interpreted as "rotational rainbow peaks," and compared with a classical hard-ellipsoid model.[57,58] This work has recently been extended to vibrationally excited NO ($v_{NO} = 5$) with Ar.[48]

In the last five years, XMB-II experiments have been performed with much higher resolution and accuracy using velocity mapping ion-imaging. Chandler and his co-workers observed the alignment and orientation of NO created by RIS with Ar as a function of a scattering angle using linearly and circularly polarized probe light.[43,139] So far, three *ab initio* calculations, the electron gas model,[132] CEPA[136] and CCSD(T) (coupled-cluster single and double excitation with a perturbative inclusion of triple excitation),[140] have been reported for the NO + Ar system. The most recent CCSD(T) surfaces calculated by Alexander successfully reproduced the spectroscopic constants

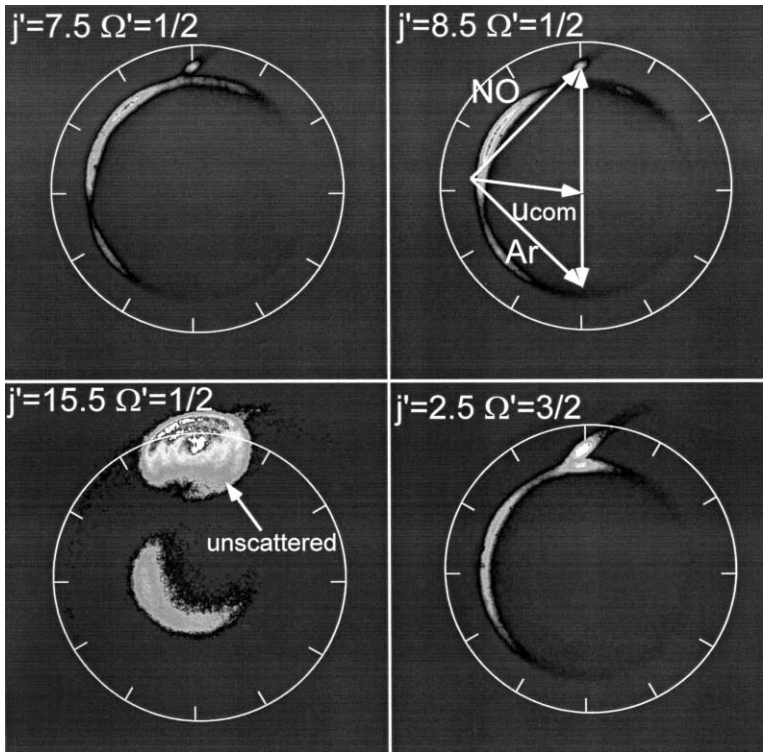

Fig. 9 Examples of the ion image observed by XMB-II (ref. 42) of $NO(^2\Pi,j'' = 0.5,\Omega'' = 1/2)$ + Ar ⟶ $NO(^2\Pi,j',\Omega' = 1/2,3/2)$ + Ar at a collision energy of 516 cm^{-1}. The final (j',Ω') states are indicated in each image. Although the Λ-doublet was not discriminated for the $(j' = 2.5,\Omega' = 3/2)$ state, the f-state was selectively observed in all other cases. A Newton diagram is superimposed on the image of $(j' = 7.5, \Omega' = 1/2)$, where the collision axis is directed vertically. The spot at the end of the $\boldsymbol{V}_{NO}$ vector is due to the unscattered NO in the beam that is populated by species exhibiting incomplete rotational cooling. Since this background signal is well separated from the scattering signal, it does not interfere with the measurement.

View Article Online

Published on 03 July 2002. Downloaded by Kyoto Daigaku on 09/09/2016 06:22:43.

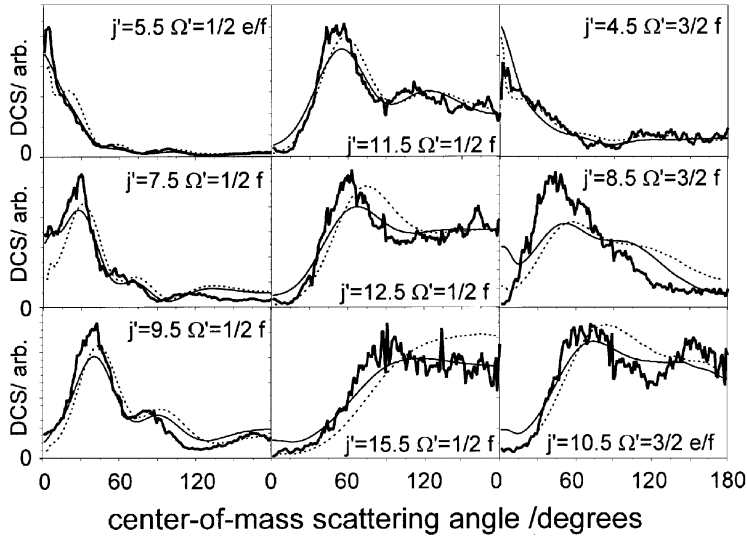

Fig. 10 SR-DCSs in RIS of NO($^2\Pi$,j'' = 0.5,Ω'' = 1/2,e + f mixture) + Ar ⟶ NO($^2\Pi$,j',Ω',e/f) + Ar at the collision energy of 516 cm^{-1}. The final states are labeled by (j',Ω',e or f) in each panel. The angular distributions measured without discrimination of the final Λ-doublet are denoted by e/f in the panel. Thick-solid lines represent the experimental distribution, while thin-solid and broken lines are the computational results using the CCSD(T) and the CEPA PESs, respectively. All of these distributions are normalized to make the integral cross sections the same in each panel. In order to compare with the experimental results, theoretical DCSs were averaged over the Λ-doublet levels in the initial (j'' = 0.5,Ω'' = 1/2) state and then smoothed with a Gaussian collision energy distribution of the 56 cm^{-1} FWHM and a Gaussian angular resolution of 8° FWHM.

of the vdW well.[118,120,140,141] The angular momentum polarization parameters observed by Chandler and his co-workers are well reproduced by close-coupling calculations using the CCSD(T) potential energy surfaces, where computations using the CEPA surfaces provide inferior agreement. Suzuki and co-workers measured the high-resolution SR-DCS at a collision energy of 516 cm^{-1}. With well-controlled molecular beam spreads that minimize the angular blurring of ion images, the observed SR-DCSs exhibit detailed features that are beyond a classical ellipsoid model (Fig. 9 and 10):[42] the observed SR-DCS with undulation sensitively changes its shape for the final (j', Ω') states. The observed SR-DCSs were compared with close-coupling calculations using the CEPA and CCSD(T) PESs (Fig. 11), where the latter provided superior agreement with the experimental result. The theoretical calculations well reproduce the general features, while a slight discrepancy was found in the small θ_{cm} region in the middle Δj of the $\Delta\Omega$ = 1 transitions, where the differences of the calculated SR-DCSs between the CEPA and CCSD(T) are discernible. The close-coupling calculations employ the rigid-rotor approximation and the R-independent spin-uncoupling and the spin–orbit couplings. These approximations have been regarded as appropriate,[136] however, a slight discrepancy between the highly accurate

View Article Online

Published on 03 July 2002. Downloaded by Kyoto Daigaku on 09/09/2016 06:22:43.

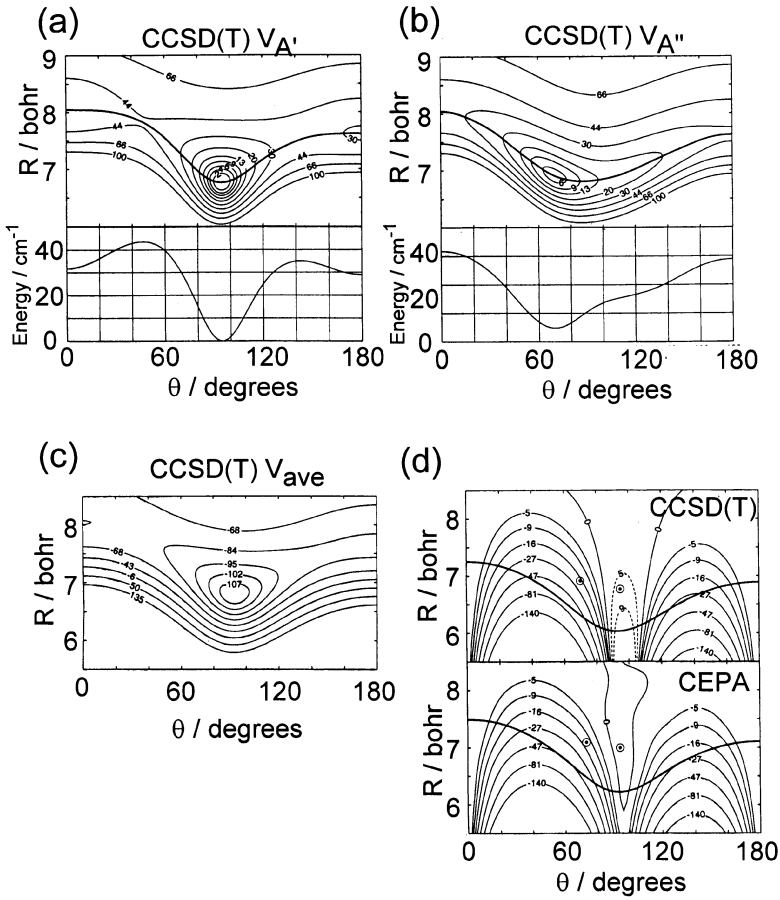

Fig. 11 The two-dimensional contour plot and one-dimensional cuts of (a) the A′ PES and (b) A″ PES for NO + Ar. The energies are in cm^{-1} with respect to the minimum of the potential. The thick line in each upper panel indicates the minimum energy orbit as a function of θ, and each lower panel shows its one-dimensional energy curve. (c) Contour plot of the average potential (V_{ave}) calculated at the CCSD(T) level. The minimum energy is -109.8 cm^{-1}. (d) Contour plot of the difference potential (V_{diff}) calculated at the CCSD(T) level and CEPA. Reproduced from ref. 140.

computations and high-resolution SR-DCS may point to the necessity of removing some of these approximations for complete agreement in the future.

7 Concluding remarks

Rotational inelastic scattering of free radicals has multi-surface nuclear dynamics, which is extremely sensitive to the topography and absolute energies of the potential energy surfaces. Experimental exploration of the dynamics involves various

View Article Online

Published on 03 July 2002. Downloaded by Kyoto Daigaku on 09/09/2016 06:22:43.

techniques for monochromatization of the initial quantum state and analysis of the final states. For the former, a supersonic expansion, optical pumping, and a hexapole state selector have been applied. As for the latter, various means such as LIF and REMPI have been employed; however, the selection of experimental observables is more important. These are the scattering distributions (DCS), the quantum state distributions, and the composite distribution of both (SR-DCS) in the order of complexity. The most detailed quantity is the SR-DCS as a composite distribution, as demonstrated for NO+Ar, where, however, the distribution is still averaged over the magnetic quantum number for the projection of j onto the space fixed axis. The experimental challenge to remove this averaging can result in the exploration of angular momentum polarization in conjunction with SR-DCS. Since an optical transition with k-photons allows the determination of the multipole moments only up to the rank $2k$, complete characterization of angular momentum polarization by optical methods is hopeless. Therefore the additional information obtainable from this approach towards to the perfect experiment depends on how the low-rank multipole moments capture the detailed features of scattering dynamics. Detection of coherence in the products is further desirable. Further improvements in SR-DCS measurements can be pursued by improving the speed spreads of molecular beams (currently $\Delta v/v = 0.05$), which would provide high-frequency oscillations in the observed SR-DCS.

The most recent XMB-II apparatus with good molecular beam intensities and a detection sensitivity required integration times of ion images in RIS of NO + Ar of the order of 10–60 min per image for all the transitions. If efficient REMPI schemes are present, the method is certainly applicable to other radical species and tests the computations at an unprecedented level of detail. Currently, no usable REMPI scheme has been found for the OH radical, which is the only roadblock to applying this method to this astronomically important species. On the other hand, remarkable agreement between the state-of-the art computations and SR-DCS measurements on NO + Ar certainly demonstrate the maturity and reliability of computational predictions of RIS. This encourages us to explore the RIS processes of various free radicals purely computationally in the near future, which is certainly the goal for experimental and theoretical chemists in the area.

If OH + H_2 RIS is not responsible for the interstellar OH maser action, there will be other important processes of free radicals as sources of population inversion. This certainly indicates the need for further investigations into the reaction dynamics of free radicals for elucidating intriguing problems in various areas.

Acknowledgements

The authors would like to thank the Ministry of Education, Science, Technology, Sports and Culture of Japan for financial support under the contract numbers (11359005, 13127204 and 13740341). TS gratefully appreciates the grant from New Energy and Industrial Technology Development Organization (NEDO) for partial support for construction of the XMB-II apparatus.

View Article Online

Published on 03 July 2002. Downloaded by Kyoto Daigaku on 09/09/2016 06:22:43.

References

1 R. T. Skodje, D. Skouteris, D. E. Manolopoulos, S. H. Lee, F. Dong and K. Liu, *Phys. Rev. Lett.*, 2000, **85**, 1206.
2 L. Schnieder, K. Seekamp-Rahn, E. Wrede and K. H. Welge, *J. Chem. Phys.*, 1997, **107**, 6175.
3 M. H. Alexander, *J. Chem. Phys.*, 1982, **76**, 5974.
4 M. H. Alexander, *J. Chem. Phys.*, 1982, **76**, 3637.
5 M. H. Alexander and P. J. Dagdigian, *J. Chem. Phys.*, 1983, **79**, 302.
6 M. H. Alexander and P. J. Dagdigian, *J. Chem. Phys.*, 1985, **83**, 2191.
7 M. H. Alexander, *Chem. Phys.*, 1985, **92**, 337.
8 G. C. Corey, M. H. Alexander and P. J. Dagdigian, *J. Chem. Phys.*, 1986, **84**, 1547.
9 MOLSCAT is a code for quantum mechanical (coupled channel) solution of the non-reactive molecular scattering problem developed by J. M. Hutson and S. Green. The code is implemented for various types of collision partners. In addition to the essentially exact close coupling method several approximate methods, including the coupled-states and infinite-order-sudden approximations, are provided.
10 HIBRIDONTM is a package of programs for the time-independent quantum treatment of inelastic collisions and photodissociation written by M. H. Alexander, D. E. Manolopoulos, H.-J. Werner, and B. Follmeg, with contributions by P. F. Vohralik, D. Lemoine, G. Corey, R. Gordon, B. Johnson, T. Orlikowski, A. Berning, A. Degli-Esposti, C. Rist, P. Dagdigian, B. Pouilly, G. van der Sanden, M. Yang, F. de Weerd and S. Gregurick.
11 X. F. Tan, P. J. Dagdigian, J. Williams and M. H. Alexander, *J. Chem. Phys.*, 2001, **114**, 8938.
12 K. Liu, R. G. Macdonald and A. F. Wagner, *Int. Rev. Phys. Chem.*, 1990, **9**, 187.
13 A. Schiffman and D. W. Chandler, *Int. Rev. Phys. Chem.*, 1995, **14**, 371.
14 J. C. Whitehead, *Rep. Prog. Phys.*, 1996, **59**, 993.
15 P. J. Dagdigian, *Chemical Dynamics and Kinetics of Small Radicals*, World Scientific, Singapore, 1995, Part 1.
16 G. Herzberg, *Molecular Spectra and Molecular Structure I. Spectra of Diatomic Molecules*, Krieger Publishing Company, Malabar, FL, 1950.
17 E. Hirota, *High-Resolution Spectroscopy of Transient Molecules*, Springer-Verlag, Berlin, 1985.
18 H. Lefebvre-Brion and R. W. Field, *Perturbations in the Spectra of Diatomic Molecules*, Academic Press, New York, 1986.
19 K. Bergmann, U. Hefter and J. Witt, *J. Chem. Phys.*, 1980, **72**, 4777.
20 U. Hefter, P. L. Jones, A. Mattheus, J. Witt, K. Bergmann and R. Schinke, *Phys. Rev. Lett.*, 1981, **46**, 915.
21 E. Gottwald, K. Bergmann and R. Schinke, *J. Chem. Phys.*, 1987, **86**, 2685.
22 E. Gottwald, A. Mattheus, K. Bergmann and R. Schinke, *J. Chem. Phys.*, 1986, **84**, 756.
23 S. D. Jons, J. E. Shirley, M. T. Vonk, C. F. Giese and W. R. Gentry, *J. Chem. Phys.*, 1996, **105**, 5397.
24 S. D. Jons, J. E. Shirley, M. T. Vonk, C. F. Giese and W. R. Gentry, *J. Chem. Phys.*, 1992, **97**, 7831.
25 G. Dharmasena, K. Copeland, J. H. Young, R. A. Lasell, T. R. Phillips, G. A. Parker and M. Keil, *J. Phys. Chem. A*, 1997, **101**, 6429.
26 G. Dharmasena, T. R. Phillips, K. N. Shokhirev, G. A. Parker and M. Keil, *J. Chem. Phys.*, 1997, **106**, 9950.
27 L. J. Rawluk, Y. B. Fan, Y. Apelblat and M. Keil, *J. Chem. Phys.*, 1991, **94**, 4205.
28 J. A. Serri, J. L. Kinsey and D. E. Pritchard, *J. Chem. Phys.*, 1981, **75**, 663.
29 J. A. Serri, C. H. Becker, M. B. Elbel, J. L. Kinsey, W. P. Moskowitz and D. E. Pritchard, *J. Chem. Phys.*, 1981, **74**, 5116.
30 B. Girard, N. Billy, G. Gouedard and J. Vigue, *J. Chem. Phys.*, 1991, **95**, 4056.
31 W. B. Chapman, M. J. Weida and D. J. Nesbitt, *J. Chem. Phys.*, 1997, **106**, 2248.
32 Z. Q. Zhao, W. B. Chapman and D. J. Nesbitt, *J. Chem. Phys.*, 1996, **104**, 3555.
33 A. J. McCaffery, K. L. Reid and B. J. Whitaker, *Phys. Rev. Lett.*, 1988, **61**, 2085.
34 K. L. Reid and A. J. McCaffery, *J. Chem. Phys.*, 1992, **96**, 5789.
35 T. L. D. Collins, A. J. McCaffery, J. P. Richardson, R. J. Wilson and M. J. Wynn, *J. Chem. Phys.*, 1995, **102**, 4419.
36 R. J. Wilson and A. J. McCaffery, *Chem. Phys. Lett.*, 1996, **261**, 195.
37 H. Meyer, *J. Chem. Phys.*, 1994, **101**, 6697.
38 H. Meyer, *J. Chem. Phys.*, 1995, **102**, 3151.
39 R. T. Skodje, D. Skouteris, D. E. Manolopoulos, S. H. Lee, F. Dong and K. Liu, *J. Chem. Phys.*, 2000, **112**, 4536.
40 L. Schnieder, W. Meier, K. H. Welge, M. N. R. Ashfold and C. M. Western, *J. Chem. Phys.*, 1990, **92**, 7027.
41 D. W. Chandler and P. L. Houston, *J. Chem. Phys.*, 1987, **87**, 1445.
42 H. Kohguchi, T. Suzuki and M. H. Alexander, *Science*, 2001, **294**, 832.
43 J. I. Cline, K. T. Lorenz, E. A. Wade, J. W. Barr and D. W. Chandler, *J. Chem. Phys.*, 2001, **115**, 6277.

View Article Online

44 K. T. Lorenz, M. S. Westley and D. W. Chandler, *Phys. Chem. Chem. Phys.*, 2000, **2**, 481.
45 A. G. Suits, L. S. Bontuyan, P. L. Houston and B. J. Whitaker, *J. Chem. Phys.*, 1992, **96**, 8618.
46 L. S. Bontuyan, A. G. Suits, P. L. Houston and B. J. Whitaker, *J. Phys. Chem.*, 1993, **97**, 6342.
47 M. S. Westley, K. T. Lorenz, D. W. Chandler and P. L. Houston, *J. Chem. Phys.*, 2001, **114**, 2669.
48 A. A. Dixit, P. J. Pisano and P. L. Houston, *J. Phys. Chem. A*, 2001, **105**, 11165.
49 T. N. Kitsopoulos, M. A. Buntine, D. P. Baldwin, R. N. Zare and D. W. Chandler, *Science*, 1993, **260**, 1605.
50 M. Ahmed, D. S. Peterka and A. G. Suits, *Chem. Phys. Lett.*, 1999, **301**, 372.
51 G. C. McBane, in *Imaging in Chemical Dynamics*, ed. A. G. Suits and R. E. Continetti, American Chemical Society, Washington, DC, 2000, ch. 13.
52 A. Eppink and D. H. Parker, *Rev. Sci. Instrum.*, 1997, **68**, 3477.
53 B. Y. Chang, R. C. Hoetzlein, J. A. Mueller, J. D. Geiser and P. L. Houston, *Rev. Sci. Instrum.*, 1998, **69**, 1665.
54 N. Yonekura, C. Gebauer, H. Kohguchi and T. Suzuki, *Rev. Sci. Instrum.*, 1999, **70**, 3265.
55 R. Schinke, *J. Phys. Chem.*, 1986, **90**, 1742.
56 R. Schinke and J. M. Bowman, *Molecular Collision Dynamics*, Springer, Berlin, 1983, ch. 4.
57 S. Bosanac, *Phys. Rev. A*, 1980, **22**, 2617.
58 S. Bosanac and U. Buck, *Chem. Phys. Lett.*, 1981, **81**, 315.
59 U. Buck, D. Otten, R. Schinke and D. Poppe, *J. Chem. Phys.*, 1985, **82**, 202.
60 S. D. Bosanac, *Chem. Phys. Lett.*, 1984, **103**, 484.
61 A. J. McCaffery, Z. T. Alwahabi, M. A. Osborne and C. J. Williams, *J. Chem. Phys.*, 1993, **98**, 4586.
62 A. J. McCaffery and R. J. Wilson, *J. Phys. B*, 1997, **30**, 5773.
63 T. W. J. Whiteley and A. J. McCaffery, *J. Chem. Phys.*, 1999, **110**, 5548.
64 A. J. McCaffery and R. J. Wilson, *Phys. Rev. Lett.*, 1996, **77**, 48.
65 H. Meyer, *Chem. Phys. Lett.*, 1994, **230**, 519.
66 K. L. Reid and A. J. McCaffery, *J. Chem. Phys.*, 1991, **95**, 4958.
67 S. L. Davis, *Chem. Phys.*, 1985, **95**, 411.
68 D. K. Hoffman, J. W. Evans and D. J. Kouri, *J. Chem. Phys.*, 1984, **80**, 144.
69 M. Faubel, *J. Chem. Phys.*, 1984, **81**, 5559.
70 H. J. Werner, B. Follmeg and M. H. Alexander, *J. Chem. Phys.*, 1988, **89**, 3139.
71 M. H. Alexander, X. Yang, P. J. Dagdigian, A. Berning and H. J. Werner, *J. Chem. Phys.*, 2000, **112**, 781.
72 G. Parlant and M. H. Alexander, *J. Chem. Phys.*, 1990, **92**, 2287.
73 P. McCabe, J. N. L. Connor and D. Sokolovski, *J. Chem. Phys.*, 1998, **108**, 5695.
74 T. W. J. Whiteley, C. Noli and J. N. L. Connor, *J. Phys. Chem. A*, 2001, **105**, 2792.
75 P. McCabe, J. N. L. Connor and D. Sokolovski, *J. Chem. Phys.*, 2001, **114**, 5194.
76 A. J. Dobbyn, P. McCabe, J. N. L. Connor and J. F. Castillo, *Phys. Chem. Chem. Phys.*, 1999, **1**, 1115.
77 C. Noli, J. N. L. Connor, N. Rougeau and C. Kubach, *Phys. Chem. Chem. Phys.*, 2001, **3**, 3946.
78 R. G. Macdonald and K. Liu, *J. Chem. Phys.*, 1989, **91**, 821.
79 R. G. Macdonald and K. Liu, *J. Phys. Chem.*, 1991, **95**, 9630.
80 R. G. Macdonald and K. Liu, *J. Chem. Phys.*, 1992, **97**, 978.
81 P. J. Dagdigian, M. H. Alexander and K. Liu, *J. Chem. Phys.*, 1989, **91**, 839.
82 M. C. van Beek, J. J. ter Meulen and M. H. Alexander, *J. Chem. Phys.*, 2000, **113**, 628.
83 A. D. Esposti and H. J. Werner, *J. Chem. Phys.*, 1990, **93**, 3351.
84 J. Klos, G. Chalasinski, M. T. Berry, R. A. Kendall, R. Burcl, M. M. Szczesniak and S. M. Cybulski, *J. Chem. Phys.*, 2000, **112**, 4952.
85 K. Schreel, J. Schleipen, A. Eppink and J. J. Ter Meulen, *J. Chem. Phys.*, 1993, **99**, 8713.
86 A. D. Esposti, A. Berning and H. J. Werner, *J. Chem. Phys.*, 1995, **103**, 2067.
87 I. J. Wysong, J. B. Jeffries and D. R. Crosley, *J. Chem. Phys.*, 1991, **94**, 7547.
88 R. A. Copeland and D. R. Crosley, *J. Chem. Phys.*, 1984, **81**, 6400.
89 D. M. Sonnenfroh, R. G. Macdonald and K. Liu, *J. Chem. Phys.*, 1991, **94**, 6508.
90 M. C. van Beek, K. Schreel and J. J. ter Meulen, *J. Chem. Phys.*, 1998, **109**, 1302.
91 M. Elitzur, *Annu. Rev. Astron. Astrophys.*, 1992, **30**, 75.
92 P. Andresen, N. Aristov, V. Beushausen, D. Hausler and H. W. Lulf, *J. Chem. Phys.*, 1991, **95**, 5763.
93 P. Andresen, D. Hausler and H. W. Lulf, *J. Chem. Phys.*, 1984, **81**, 571.
94 D. P. Dewangan, D. R. Flower and G. Danby, *J. Phys. B: At. Mol. Opt. Phys.*, 1986, **19**, L747.
95 R. Schinke and P. Andresen, *J. Chem. Phys.*, 1984, **81**, 5644.
96 E. Kochanski and D. R. Flower, *Chem. Phys.*, 1981, **57**, 217.
97 K. Schreel and J. J. ter Meulen, *J. Chem. Phys.*, 1996, **105**, 4522.
98 A. R. Offer, M. C. Vanhemert and E. F. Vandishoeck, *J. Chem. Phys.*, 1994, **100**, 362.
99 A. R. Offer and M. C. Vanhemert, *J. Chem. Phys.*, 1993, **99**, 3836.

Published on 03 July 2002. Downloaded by Kyoto Daigaku on 09/09/2016 06:22:43.

View Article Online

Published on 03 July 2002. Downloaded by Kyoto Daigaku on 09/09/2016 06:22:43.

100 P. J. Dagdigian, *Annu. Rev. Phys. Chem.*, 1997, **48**, 95.
101 C. Ottinger, R. Velasco and R. N. Zare, *J. Chem. Phys.*, 1970, **52**, 1636.
102 K. Bergmann and W. Demtröder, *J. Phys. B*, 1972, **5**, 1386.
103 K. Bergmann, H. Klar and W. Schlecht, *Chem. Phys. Lett.*, 1972, **12**, 522.
104 C. Ottinger, *Chem. Phys.*, 1973, **1**, 161.
105 D. Poppe, *Chem. Phys. Lett.*, 1973, **1**, 63.
106 H. Klar, *J. Phys. B*, 1973, **6**, 2139.
107 S. Green and R. N. Zare, *Chem. Phys.*, 1975, **7**, 62.
108 R. N. Dixon, D. Field and R. N. Zare, *Chem. Phys. Lett.*, 1985, **122**, 310.
109 M. H. Alexander and P. J. Dagdigian, *J. Chem. Phys.*, 1984, **80**, 4325.
110 M. H. Alexander, P. Andresen, R. Bacis, R. Bersohn, F. J. Comes, P. J. Dagdigian, R. N. Dixon, R. W. Field, G. W. Flynn, K. H. Gericke, E. R. Grant, B. J. Howard, J. R. Huber, D. S. King, J. L. Kinsey, K. Kleinermanns, K. Kuchitsu, A. C. Luntz, A. J. McCaffery, B. Pouilly, H. Reisler, S. Rosenwaks, E. W. Rothe, M. Shapiro, J. P. Simons, R. Vasudev, J. R. Wiesenfeld, C. Wittig and R. N. Zare, *J. Chem. Phys.*, 1988, **89**, 1749.
111 J. M. Brown, J. T. Hougen, K.-P. Huber, J. W. C. Johns, I. Kopp, H. Lefebvre-Brion, A. J. Merer, D. A. Ramsay, J. Rostas and R. N. Zare, *J. Mol. Spectrosc.*, 1975, **55**, 500.
112 M. H. Alexander, S. L. Davis and P. J. Dagdigian, *J. Chem. Phys.*, 1985, **83**, 556.
113 S. J. Bullman and P. J. Dagdigian, *J. Chem. Phys.*, 1984, **81**, 3347.
114 P. J. Dagdigian and S. J. Bullman, *J. Chem. Phys.*, 1985, **82**, 1341.
115 S. L. Davis, B. Pouilly and M. H. Alexander, *Chem. Phys.*, 1984, **91**, 81.
116 G. C. Corey and F. R. McCourt, *J. Phys. Chem.*, 1983, **87**, 2723.
117 S. J. Bullman and P. J. Dagdigian, *Chem. Phys.*, 1984, **88**, 479.
118 P. D. A. Mills, C. M. Western and B. J. Howard, *J. Phys. Chem.*, 1986, **90**, 4961.
119 P. D. A. Mills, C. M. Western and B. J. Howard, *J. Phys. Chem.*, 1986, **90**, 3331.
120 K. Tsuji, K. Shibuya and K. Obi, *J. Chem. Phys.*, 1994, **100**, 5441.
121 Y. Kim, K. Patton, J. Fleniken and H. Meyer, *Chem. Phys. Lett.*, 2000, **318**, 522.
122 Y. Kim, J. Fleniken and H. Meyer, *J. Chem. Phys.*, 2001, **114**, 5577.
123 H. H. W. Thuis, S. Stolte, J. Reuss, J. J. H. van den Biesen and C. J. N. van den Meijdenberg, *Chem. Phys.*, 1980, **52**, 211.
124 H. Thuis, S. Stolte and J. Reuss, *Chem. Phys.*, 1979, **43**, 351.
125 M. J. L. de Lange, M. Drabbels, P. T. Griffiths, J. Bulthuis, S. Stolte and J. G. Snijders, *Chem. Phys. Lett.*, 1999, **313**, 491.
126 J. J. van Leuken, F. H. W. Vanamerom, J. Bulthuis, J. G. Snijders and S. Stolte, *J. Phys. Chem.*, 1995, **99**, 15573.
127 J. J. van Leuken, J. Bulthuis, S. Stolte and J. G. Snijders, *Chem. Phys. Lett.*, 1996, **260**, 595.
128 M. H. Alexander and S. Stolte, *J. Chem. Phys.*, 2000, **112**, 8017.
129 P. Casavecchia, A. Lagana and G. G. Volpi, *Chem. Phys. Lett.*, 1984, **112**, 445.
130 P. Andresen, H. Joswig, H. Pauly and R. Schinke, *J. Chem. Phys.*, 1982, **77**, 2204.
131 H. Joswig, P. Andresen and R. Schinke, *J. Chem. Phys.*, 1986, **85**, 1904.
132 G. C. Nielson, G. A. Parker and R. T. Pack, *J. Chem. Phys.*, 1977, **66**, 1396.
133 C. R. Bieler, A. Sanov and H. Reisler, *Chem. Phys. Lett.*, 1995, **235**, 175.
134 M. Drabbels, A. M. Wodtke, M. Yang and M. H. Alexander, *J. Phys. Chem. A*, 1997, **101**, 6463.
135 A. Lin, S. Antonova, A. P. Tsakotellis and G. C. McBane, *J. Phys. Chem. A*, 1999, **103**, 1198.
136 M. H. Alexander, *J. Chem. Phys.*, 1993, **99**, 7725.
137 M. T. Vonk, J. A. Bacon, C. F. Giese and W. R. Gentry, *J. Chem. Phys.*, 1997, **106**, 1353.
138 J. A. Bacon, C. F. Giese and W. R. Gentry, *J. Chem. Phys.*, 1998, **108**, 3127.
139 K. T. Lorenz, D. W. Chandler, J. W. Barr, W. W. Chen, G. L. Barnes and J. I. Cline, *Science*, 2001, **293**, 2063.
140 M. H. Alexander, *J. Chem. Phys.*, 1999, **111**, 7426.
141 Y. Kim, J. Fleniken, H. Meyer, M. H. Alexander and P. J. Dagdigian, *J. Chem. Phys.*, 2000, **113**, 73.
142 G. Hall, K. Liu, M. J. McAuliffe, C. F. Giese and W. R. Gentry, *J. Chem. Phys.*, 1986, **84**, 1402.
143 M. C. van Beek, J. J. ter Meulen and M. H. Alexander, *J. Chem. Phys.*, 2000, **113**, 637.
144 M. C. van Beek and J. J. ter Meulen, *J. Chem. Phys.*, 2001, **115**, 1843.
145 M. C. van Beek, G. Berden, H. L. Bethlem and J. J. ter Meulen, *Phys. Rev. Lett.*, 2001, **86**, 4001.
146 L. H. Lai, Y. H. Chiu and K. Liu, *J. Chem. Phys.*, 1995, **103**, 8492.
147 R. G. Macdonald and K. Liu, *Abstr. Pap. Am. Chem. Soc.*, 1992, **203**, 196.
148 P. L. James, I. R. Sims and I. W. M. Smith, *Chem. Phys. Lett.*, 1997, **272**, 412.
149 M. Islam, I. W. M. Smith and J. W. Wiebrecht, *J. Chem. Phys.*, 1995, **103**, 9676.
150 R. G. Macdonald and K. Liu, *J. Chem. Phys.*, 1990, **93**, 2431.
151 R. Fei, H. M. Lambert, T. Carrington, S. V. Filseth, C. M. Sadowski and C. H. Dugan, *J. Chem. Phys.*, 1994, **100**, 1190.
152 R. Fei, D. E. Adelman, T. Carrington, C. H. Dugan and S. V. Filseth, *Chem. Phys. Lett.*, 1995, **232**, 547.
153 P. J. Dagdigian, *J. Chem. Phys.*, 1989, **90**, 6110.

View Article Online

Published on 03 July 2002. Downloaded by Kyoto Daigaku on 09/09/2016 06:22:43.

View Article Online

Published on 03 July 2002. Downloaded by Kyoto Daigaku on 09/09/2016 06:22:43.

View Article Online

Published on 03 July 2002. Downloaded by Kyoto Daigaku on 09/09/2016 06:22:43.